ADVANCED FUNCTIONAL MATERIALS
www.afm-journal.de

Deconstructing 3D Structured Materials by Modern Ultramicrotomy for Multimodal Imaging and Volume Analysis across Length Scales

Irene Wacker, Ronald Curticean, Daniel Ryklin, Britta Weidinger, Frederik Mayer, Li-Yu Huang, Julian Hoffmann, Monsur Islam, Nadine von Coelln, Tanja Schmitt, Christian Huck, Petra Tegeder, Florian Feist, Jochen A. Kammerer, Christopher Barner-Kowollik, Martin Wegener, Eva Blasco, Ulrich Gengenbach, and Rasmus R. Schröder**

Based on the rapid advances in additive manufacturing, micro-patterned heterostructures of soft materials have become available that need to be characterized down to the nanoscale. Advanced function-structure relationships are designed by direct 3D structuring of the object and – in the future – fine control over material functionality in 3D will produce complex functional objects. To control their design, fabrication and final structure, morphological and spectroscopical imaging in 3D at nanometer resolution are critically required. With examples of carbon-based objects, it is demonstrated how serial ultramicrotomy, that is, cutting a large number of successive ultrathin sections, can be utilized to gain access to the interior of 3D objects. Array tomography, hierarchical imaging and correlative light and electron microscopy can bridge length scales over several orders of magnitude and provide multimodal information of the sample's inner structure. Morphology data derived from scanning electron microscopy are correlated with spectroscopy in analytical transmission electron microscopy and probe microscopy at nanometer resolution, using TEM-electron energy loss spectroscopy and infrared-scanning-near-field microscopy. The correlation of different imaging modalities and spectroscopy of carbon-based materials in 3D provides a powerful toolbox of complementary techniques for understanding emerging functions from nanoscopic structuring.

1. Introduction

A fascinating aspect of modern materials is their complexity based on material blends or chemically structured 3D compositions. Some of the recently published meta-materials[1] gain their extraordinary properties from their specifically designed 3D structures and it is foreseeable that further developments in 3D printing of the underpinning material building blocks will allow ever finer structures to be prepared. Thus, the characterization of the resulting new objects in their material, function and – equally important – in their structure and chemical composition at nanometer-resolution in three dimensions is critical. The visualization of such design parameters will aid in defining and optimizing the processing of novel materials into their functional structure, along with providing necessary information, for example, for future rational design or processing steps. The recent progress in 3D laser

I. Wacker, R. Curticean, D. Ryklin, R. R. Schröder
3DMM2O
Cluster of Excellence and BioQuant
Universität Heidelberg
Im Neuenheimer Feld 267, 69120 Heidelberg, Germany
E-mail: irene.wacker@bioquant.uni-heidelberg.de;
rasmus.schroeder@bioquant.uni-heidelberg.de

The ORCID identification number(s) for the author(s) of this article can be found under https://doi.org/10.1002/adfm.202302025

DOI: 10.1002/adfm.202302025

B. Weidinger, E. Blasco
3DMM2O
Cluster of Excellence and IMSEAM
Universität Heidelberg
Im Neuenheimer Feld 225, 69120 Heidelberg, Germany

F. Mayer, F. Feist, C. Barner-Kowollik, M. Wegener
3DMM2O
Cluster of Excellence and Institute of Nanotechnology (INT)
Karlsruhe Institute of Technology (KIT)
76344 Eggenstein-Leopoldshafen, Germany

microprinting allows for the manufacturing of complex objects with feature sizes down to 50–100 nm.[2] To benchmark and further optimize the printing processes it is paramount to characterize the printed polymer objects in detail at their nanoscale, that is, with a spatial – and also chemical – resolution of better than about 10–20 nm. Traditional scanning electron microscope (SEM) analysis of sputter-coated structures may be sufficient for a first impression whether the printing quality is adequate, while providing only information about the printed object's outer surfaces. Examining – for example – homogeneity of the structuring in a printed object's interior is not possible with that approach. Other readily available techniques such as, for example, X-ray micro-computed tomography (μCT) do not provide the necessary spatial resolution or chemical information. Even state-of-the-art research nano-CT setups with a voxel size as small as about 50 nm are limited in resolution to typically 100–150 nm, obtained there for a small specimen volume of 20 × 20 × 12 μm — the specimen being prepared by focused ion beam milling to achieve the small size required for this level of resolution.[3]

Therefore, the techniques of choice are electron microscopy and different analytical probe microscopies. However, to observe the inside of an object, it first needs to be made accessible for imaging, ideally in a controlled way, producing a smooth surface amenable even to quantitative analytical analysis. Herein, we discuss ultramicrotomy for such a task: It has been shown, for example, that the distribution of pores produced by phase separation from a modified photoresist can be visualized with this technique.[2a]

In general, ultramicrotomy is a way to deconstruct a material into ultrathin (60–200 nm) sections with the help of a diamond knife. Ultramicrotomy has originally been introduced to dissect biological material, such as tissue and cells, for ultrastructural analysis by transmission electron microscopy (TEM), but has since also been applied in materials science for TEM analysis of many different materials.[4] Since the material has to be sectioned with a diamond knife, very hard or brittle materials may not be suitable, except in some rare cases.[4] On the other hand, soft materials such as tissue or hydrogels, cannot be sectioned directly. Such materials may be impregnated with a suitable resin, for example, epoxide or acrylic resins, and easily sectioned after curing by heat or UV light.

A particular challenge of morphological characterization is the analysis of a large volume of a material that is non-uniform, possessing asymmetry, anisotropy, or irregular domain distributions. In such cases it is not sufficient to analyze a small number of sections. Instead, it is necessary to inspect an extended volume, ideally in a hierarchical manner across length scales, from macro- via micro- to nano-dimensions.

There are several ways to approach the dissection, many of them pioneered by the neurobiologists' quest to map brains, resulting in the rise of so-called volume electron microscopy.[5] One possibility is serial block face scanning electron microscopy (SBFSEM) where the block face, that is, the surface of the trimmed sample (cf. Figure S1, Supporting Information), is first imaged with the electron beam. Subsequently a thin slice is cut off with a diamond knife installed in the specimen chamber of an SEM. The newly exposed surface is scanned again with the electron beam. These two process steps are repeated for hundreds or thousands of cycles, creating a 3D representation of the sample.[6] The method has been applied to investigate corrosion sites in aluminum and magnesium alloys.[7] Using an energy dispersive spectroscopy detector, it is further possible to combine element specific mapping with SBFSEM.[8] For less ductile materials that cannot be cut with a diamond knife the instrument of choice is a focused ion beam scanning electron microscope (FIBSEM). Here an ion or plasma beam, most commonly composed of gallium ions, is used instead of a physical knife to remove the imaged top layer from a material block. Repeating cycles of imaging and ion milling are used to produce a stack of images (ref. [8] for more details).

An obvious drawback of both SBFSEM and FIBSEM, is the fact that they are destructive: The material layers that are removed by sectioning or milling will disappear irretrievably into the specimen chamber of the SEM, precluding further investigations of the sample at a later point in time, for example, with higher resolution or correlated imaging or analytical techniques. To circumvent the above problem, we are using another 3D approach, called array tomography (AT). Here, the sample is sectioned in a conventional ultramicrotome and ribbons of large numbers of serial sections are deposited on solid supports, such as pieces of silicon wafer or glass coverslips.[9] These can subsequently be imaged either with a light microscope (LM), a probe microscope, or SEM, or a combination, in a correlated fashion.

In the following, we demonstrate how AT can be utilized to adapt workflows for 3D structural characterization of organic and inorganic carbon materials with different complexities using three case studies. We illustrate different elements of the corresponding workflows including staining strategies, embedding, imaging and image processing. Another aspect of modern ultramicrotomy, the use of an oscillating knife, is illustrated in a fourth case study and will extend the applicable imaging modes to analytical TEM.

2. Results

To demonstrate what information about a given material may become available when using ultramicrotomy we will first discuss typical workflows leading to a variety of imaging regimes that can

L.-Y. Huang, J. Hoffmann, U. Gengenbach
Institute for Automation and Applied Informatics
Karlsruhe Institute of Technology (KIT)
76344 Eggenstein-Leopoldshafen, Germany

M. Islam
3DMM2O
Cluster of Excellence and Institute of
Microstructure Technology (IMT)
Karlsruhe Institute of Technology (KIT)
76128 Karlsruhe, Germany

N. von Coelln, T. Schmitt, C. Huck, P. Tegeder
3DMM2O
Cluster of Excellence and Physikalisch-Chemisches Institut
Universität Heidelberg
Im Neuenheimer Feld 253, 69120 Heidelberg, Germany

J. A. Kammerer, C. Barner-Kowollik
School of Chemistry and Physics
Centre for Materials Science
Queensland University of Technology (QUT)
2 George Street, Brisbane City, QLD 4000, Australia

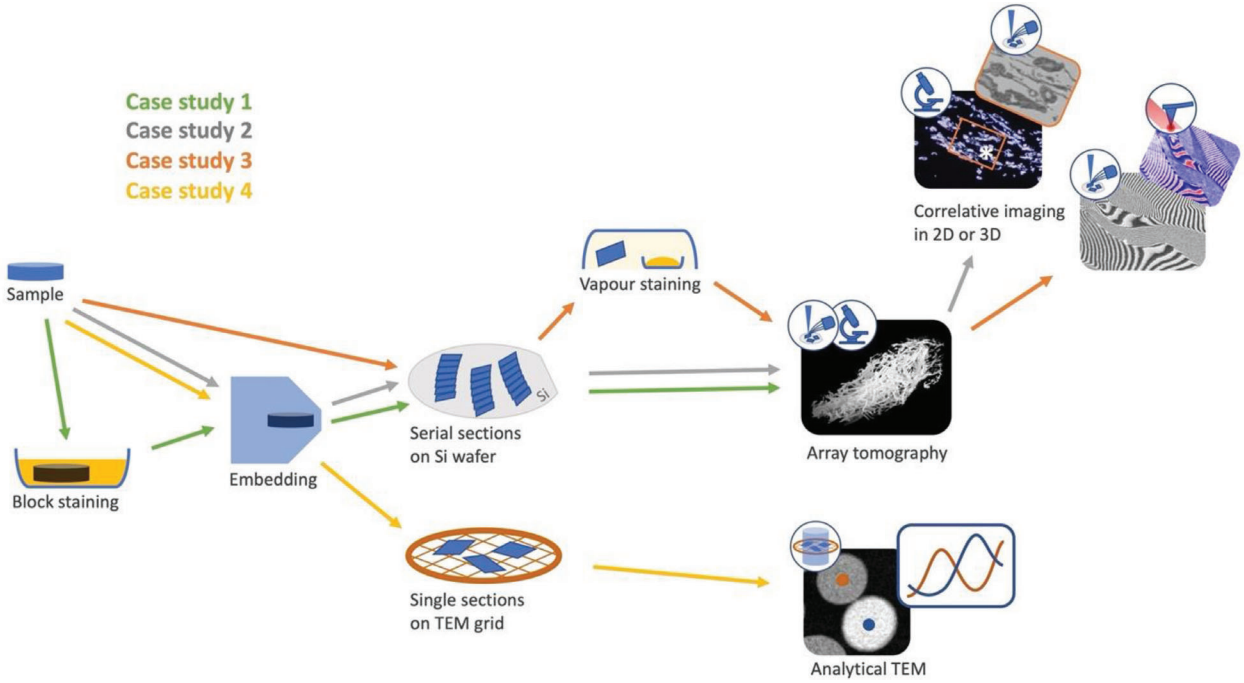

Figure 1. Typical processing workflows for carbon materials. First, samples are embedded in epoxy resin either directly (case studies 2 and 4) or after staining (case study 1). Sections cut with an ultramicrotome are placed on pieces of Silicon wafer or on metal grids. Single sections on wafers may be imaged by either LM or SEM or analyzed in a correlated way using both modalities (CLEM, see also Figure 2 / case study 1). The same is possible for serial sections on wafers, an approach known as Array Tomography, AT, in the biosciences because it can be used to reconstruct the sample's 3D structure by combining the images of all serial sections into a common volume (case studies 1 and 2). Another possibility for examining sections is the correlation of SEM data with probe microscopy. This is demonstrated here using IR-SNOM in case study 3. An alternative, very convenient way to introduce contrast, is vapor staining of already cut sections. This will be used in case study 3 to distinguish the different components of a block-copolymer. Finally, sections placed on grids can be characterized by analytical TEM, in case study 4 by electron energy loss spectroscopy, EELS.

also be combined. With a total of four case studies we will then illustrate different possibilities. Examples of three organic carbon-based materials, already being used or meant to be used for 3D-printing will be introduced. They range from a modification of a well-studied photoresist system in case study 1 over a pyrolyzed material in case study 2 and a block-copolymer in case study 3 to newly developed functional microparticles in case study 4.

2.1. Typical Workflows

A typical workflow includes sample preparation, sectioning, and imaging (**Figure 1**). For ultramicrotomy sectioning, samples need to have a certain macroscopic size to allow clamping into a sample holder for sectioning (cf. Figure S1, Supporting Information). If the sample is large enough to be directly clamped into a – so-called – flat specimen holder (Figure S1E, Supporting Information) it can be trimmed and sectioned directly.

Microscale samples, such as the polymer cylinder produced from an acrylate-based photoresist in Figure S1A, Supporting Information are usually embedded into a resin, here an epoxide (Figure S1D, Supporting Information) to make handling possible. To create contrast between the polymer sample and the embedding resin the sample may be stained before the embedding step by impregnating it with some heavy-metal compound (Figure S1A, Supporting Information). However, staining agents can also be applied to the sections using vapor from the solution of a reactive heavy metal oxide (Figure 1). In our case studies we have used OsO_4 and RuO_4 as staining agents.

Before sectioning, the sample is trimmed to create a block-face of typically less than 1 mm in each direction (Figure S1G–I, Supporting Information). With a diamond knife, 60–200 nm thick sections are cut and placed on a substrate for LM and SEM imaging, or on grids for TEM analysis. Depending on the research question to be answered, a few single sections may be sufficient. If extensive 3D characterization is desired, serial sectioning is performed.

Characterization of the sections is possible in several ways: If deposited on glass coverslips or slides they may be imaged in an ordinary LM, but SEM imaging then requires sputter coating of the entire sample-substrate assembly to prevent charging by the electron beam. When using n-doped silicon wafers as substrate for section deposition charging can be avoided because the sections are so thin (≈100 nm) that potentially induced negative charges are able to dissipate into the silicon. However, if correlation between light and electron microscopy (CLEM) is desired, an LM with epi-illumination is used (see, e.g., case study 1). Investigation of a larger volume, potentially even an entire printed sample, is done by AT, using serial sections and imaging them in either LM or SEM or correlating both modalities (Figure 1). While simple AT workflows are increasingly used in a biomedical or cell biological setting, their application and the possibilities they offer

for a correlative analysis have not yet been described for materials. From our experience with resin embedded biological samples it is obvious that an adaption of the method will be most suitable for carbon materials. Examples herein are case studies 2 and 3. Since the sections' surface is rather flat, they are also suitable for scanning probe microscopy, such as scanning near-field microscopy (SNOM) or atomic force microscopy (AFM). We show a correlation between infrared (IR) scanning-SNOM and SEM on the same region of an ultrathin section in case study 3. Finally, ultrathin sectioning has long been used to characterize materials in the TEM – we focus here on an analytical method using electron energy loss spectroscopy (EELS) in case study 4.

2.2. Case Study 1 – using CLEM and AT to Optimize 3D Laser Nanoprinting of an Acrylate-Based Photoresist Producing Porous Objects

When developing a photoresist that would combine self-assembly with 3D laser micro-printing and produce inherently porous objects, we realized that we needed a reliable way of benchmarking the printed objects' interior.[2] Due to their porosity the objects could not be sectioned directly but had to be infiltrated with another resin to prevent collapse during the sectioning process. To distinguish the printed polymer cylinder (Figure S1A, Supporting Information top) from the embedding resin, we first treated it with OsO_4 which binds to residual double-bonds in the photoresist and stains the entire object black (Figure S1, Supporting Information bottom). After embedding, the stained cylinder is readily visible in the yellowish epoxide block (Figure S1D, Supporting Information). Single sections of a cylinder from early printing attempts – which looked fine from the outside – were first imaged with darkfield epi-illumination in a LM (**Figure 2**A) and then in a SEM (Figure 2B). As is already obvious in the LM image, the cross section does not display a homogeneous porosity, but shows very fluffy material on top of the structure and a porosity gradient in the cylinder itself. Generally, the porosity seems lower along the outside of the cylinder and higher in its center. Using hierarchical imaging in the SEM, we confirmed this impression by first recording an image with intermediate magnification (30 nm pixel size) of a region of interest (ROI) extending from the fluffy top to the bottom of the cylinder's cross section (Figure 2C). Within that segment, we placed three more ROIs to be imaged with highest resolution (5 nm pixel size) at the bottom, center, and top of the structure (Figure 2D–F, respectively). There are indeed major differences in porosity between the three locations. To exclude that this result was induced by our sample preparation – perhaps by the epoxide resin not penetrating evenly and thus not filling more central pores – we broke a cylinder into two halves after staining it with OsO_4 and imaged the fracture face with SEM (Figure S2A,B, Supporting Information). It is obvious that even without embedding differences in porosity can be observed, again with denser material at the edges and more porous material in the center of the sample. The fracture face of a fully native sample without any staining is shown in Figure S2C, Supporting Information. Imaging of a pure polymer sample is more difficult than of a sample impregnated with heavy metal due to charging, therefore the image is rather noisy. Still, a clear difference in porosity between edge and center can be seen (Figure S2D, Supporting Information). Taking all these findings together indicate that the differences in porosity were caused by the printing process which was not yet sufficiently controlled.

After confirming by CLEM on the same section that we could judge the overall quality of the printed structure already in the LM, further optimization steps could be validated much faster by using that imaging mode for screening.

As demonstrated in the original paper, pore sizes could be controlled by varying the laser power.[2] To check the homogeneity of pore sizes not just on one section, but in a larger volume, we used AT. 3D reconstructions from segments of structures written with two different laser power settings of 30 mW or 45 mW are shown in Figure 2I as 3D rendering. Corresponding details from single sections within the volume are displayed in Figure 2G,H, respectively. The inset in Figure 2G, recorded with darkfield LM, shows that the overall porosity of objects printed after optimization of the printing process was very uniform.

It should be noted that comparable 3D datasets at high resolution (5 nm pixel size) might also be created by FIBSEM,[10] but this method would not allow comprehensive characterization of a large structure, since the volume that can be milled and imaged is limited due to technical reasons. With conventional FIBSEM instruments a volume of about 1000 μm^3 at 5–8 nm voxel size is routinely achievable.[11] Knowing that in early printing attempts very different pore sizes within one cylinder were observed, depending on where the region of interest (ROI) was placed, analysis with FIBSEM would have been difficult. It would either have produced statistically unreliable results or a very precise targeting of the milling volume would have been necessary to sample all the different porosities in a representative manner.

With AT however it is possible to slice up an entire printed structure and visualize it in a correlated and hierarchical manner.

2.3. Case Study 2 – 3D CLEM to Target a Sub-Volume for SEM Recording from an Extended LM Reconstructed Volume

Pyrolysis of 3D objects can be used to decrease their feature size.[12] In this process, organic carbon materials – such as polymers – are converted into inorganic pyrolytic carbon materials, including amorphous or glassy carbon, depending on the pyrolysis protocol, mainly on the final pyrolysis temperature.

To demonstrate how targeting of certain interesting features in such an object might work, we chose a carbon origami structure, obtained from pyrolyzing an origami-folded cellulose paper and featuring a randomly distributed carbon microfiber network (see ref.[13] for detailed fabrication). A small piece from the carbon origami structure was embedded in Spurr's resin.

To keep the sample in a well-defined orientation for sectioning, a 3D-printed polymer fork – the green structure in **Figure 3**A – is designed in such a way (see also the design files as available from SI) that it fits exactly into the embedding mold and thus prevents movement of the sample during heat polymerization. In our work such geometrically constrained embedding proved to be advantageous when cutting serial sections relative to a defined sample axis. After polymerization and trimming (cf. Figure S1, Supporting Information) 1045 serial sections were cut in a fully automated way.[14] In brief, 19 ribbons of 55 sections each were

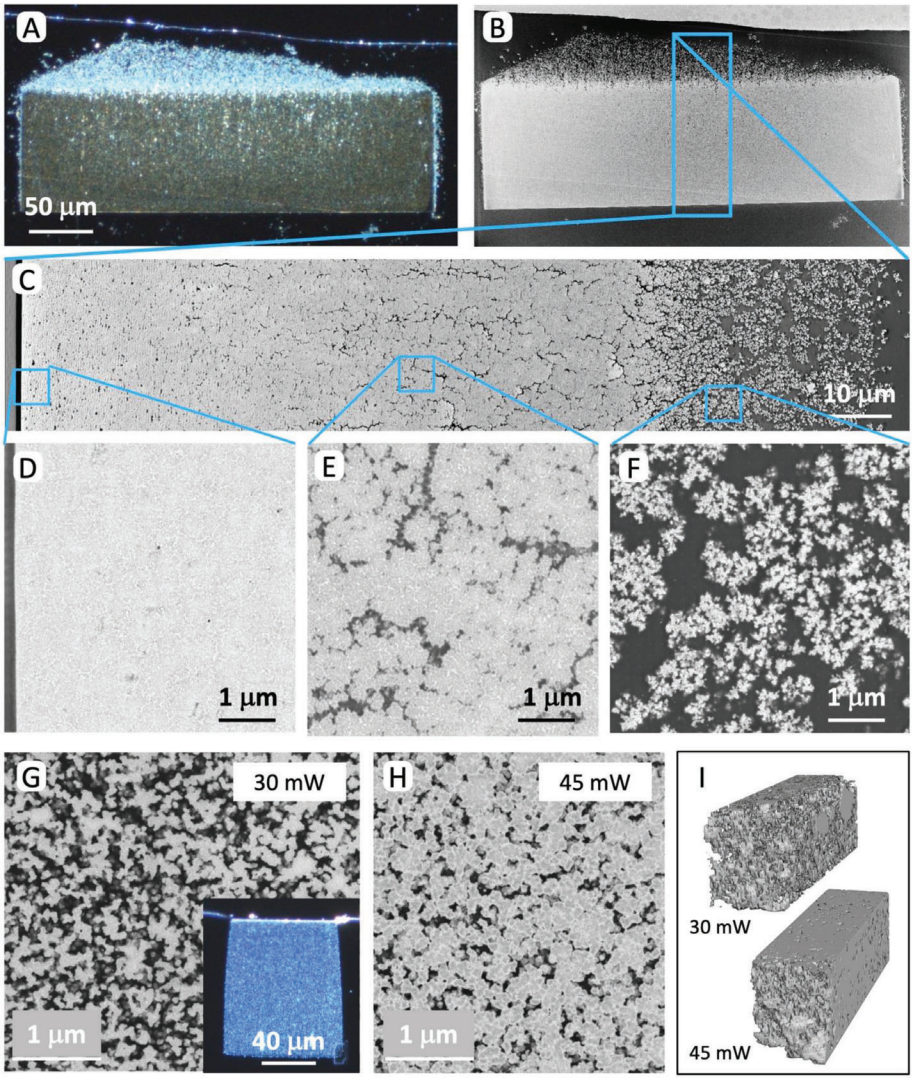

Figure 2. (Case study 1) Introducing CLEM, hierarchical imaging, and AT. A porous cylinder made by 3D laser printing was stained with OsO_4 and embedded in epoxide resin (cf. Figure S1A,D, Supporting Information). Single sections were analyzed with darkfield light microscopy in epi-illumination mode A) and with SEM using the InLens secondary electron detector (B–F). Hierarchical imaging of the entire cross section (B) with a pixel size of 400 nm, of a central segment (C) with a pixel size of 30 nm, and of selected details (D–F) with a pixel size of 5 nm. Serial section analysis of structures fabricated after optimization of the printing process using 30 mW (G) or 45 mW (H) laser power. Inset in G shows darkfield image of cross section through entire structure. Volume rendering of corresponding 3D reconstructions (I) show decreasing porosity with increasing laser power, see also movie 2 in SI.

distributed on three pieces (22 × 22 mm) cut from a silicon wafer (Figure 3B) each of which had been functionalized by silanization and plasma treatment to create a pattern of hydrophilic channels into which the section ribbons are being fed. Applying darkfield epi-illumination LM (Figure 3C) images of all 1045 sections were acquired using automated imaging (correlated array tomography (CAT) module of ZEN imaging software, cf. SI), aligned using the TrakEM module of the image analysis software FIJI[15] and visualized in Chimera[16] (Figure 3D and Movie S3, Supporting Information). A region of interest (orange box in Figure 3C) exhibiting lamellar features (asterisk) in addition to the expected donut shapes resulting from the hollow cellulose fibers (arrowheads in Figure 3E) was selected in this LM volume. The corresponding sub-volume, extending over 110 sections was imaged in the SEM with 30 nm pixel size (representative slice in Figure 3E) and reconstructed as above (Figure 3F, Movie S4, Supporting Information)).

This example illustrates that even large volumes – here a volume of 1 mm × 0.4 mm in the xy-plane (block-face) and 0.2 mm in the z-direction (1045 sections of 200 nm thickness each) – has been cut and analyzed by full automation of sectioning and imaging, in both, light and electron microscopy. To evaluate the time efficiency of that approach, **Table 1** gives a compilation of the times required for each step.

Figure S4, Supporting Information provides additional details. The advantage of prescreening the entire volume in the LM and defining interesting features there becomes immediately obvious when considering that it would have taken 35 h to record the

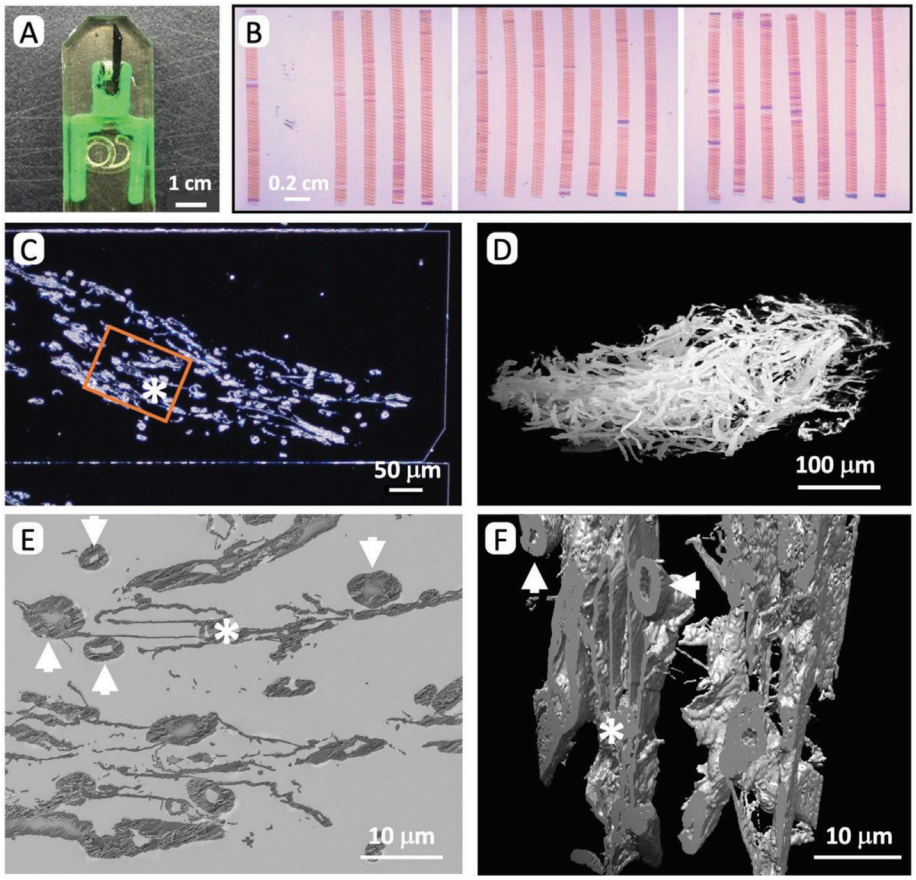

Figure 3. (Case study 2) Targeting a sub-volume from a large 3D reconstruction based on light microscopy data. A piece of pyrolyzed paper origami was embedded in Spurr's resin using a 3D-printed fork (green object) as holder to prevent re-orientation of the sample in the resin block during polymerization A). 1045 serial sections (100 nm thick) were cut in a fully automated, computer-controlled process and distributed on three pieces of silicon wafer (22 × 22 mm) (B). All three pieces were imaged in a light microscope using darkfield epi-illumination mode, with a representative section shown in (C) and the rendering of the corresponding 3D reconstruction in (D). A series of 110 images containing the ROI marked in orange in (C) was recorded in a SEM using secondary electron detectors. A representative section is shown in (E) and the corresponding 3D rendering of the reconstruction in (F). See also Supporting Information for movies of both 3D reconstructions. Asterisk indicates three stacked lamellae, arrowheads cross sections of hollow fibers.

entire stack (cf. Table comment [a] estimated SEM image capturing time) in the SEM instead about 8 h in the LM. A further advantage is that LM imaging does not have an adverse influence on the sections, for example, there is no beam damage or contamination.

2.4. Case Study 3 – Analyzing Domain Boundaries and Defects in a Block-Copolymer in 3D and Correlating SEM with IR-SNOM Data

Block copolymers are very attractive materials due to their potential to self-assemble in ordered periodic nanostructures being promising candidates for several applications ranging from membranes and drug delivery to templating for nanofabrication.[17] The self-assembled nanostructures have thoroughly been investigated for thin films. However, less attention has been paid to bulk morphologies in 3D. Herein, to establish how to analyze short- or long-range order and to characterize defects and domain boundaries in the bulk, we started out with an ≈1–2 mm thick film of a solvent-annealed block-copolymer consisting of PS and P(MMA-HEMA). Thin slivers cut from such a film (Figure S1B, Supporting Information) were embedded into Spurr's epoxy resin without further staining (Figure S1C, Supporting Information). Single or serial sections on silicon wafers pieces were stained in the vapor phase of an aqueous RuO_4 solution in a closed chamber. It is known that RuO_4 can react with the aromatic systems of PS,[18] creating a selective metal stain for this component that in turn produces a strong signal in the SEM with both, secondary electron (SE) and backscattered electron (BSE) detectors. Since PMMA was described as non-binding to RuO_4, it should interact less with electrons and thus appear with a low counting signal, in our images visible as a dark material. This vapor staining from an aqueous solution has the advantage that the sample is not in contact with an organic solvent, which otherwise could also change its structure (solvent vapor annealing).

To confirm the assignment of materials in the SEM, we performed IR-SNOM and SEM measurements on the same regions. When irradiating the block-copolymer with IR-SNOM at a PMMA absorption band (1152 cm^{-1}, cf. Figure S5, Supporting Information), a high IR-SNOM phase signal is observed for

the regions which appear black in SEM and a low IR-SNOM phase signal for the regions which appear white in SEM (cf. **Figure 4**A,C). This confirms that vapor-phase staining with RuO_4 indeed creates a specific metal stain for polystyrene. Probing with IR-SNOM at 1602 cm^{-1} wavenumber (see Figure 4B), corresponding to a PS absorption band (Figure S5, Supporting Information), a relative phase switch compared to 1152 cm^{-1} (PMMA) is observed.

Large scan fields (up to 30 × 50 µm) recorded from serial sections produced with the method introduced in case study 2 show the desired lamellar organization with lamellae in various orientations, presumably with domain boundaries between different orientations, and a number of additional defects. However, closer inspection – especially in 3D – shows that the lamellar ordering is continuous across most of the presumed domain boundaries – while a smaller number of orientation boundaries indeed have disrupted lamellae. An example of these two types of boundaries is shown in Figure 4D–O where closely spaced lamellae (right side of image) transition into a region of obliquely sectioned, more disordered lamellae with apparently wider spacings (left side). In contrast to this continuous orientational transition, complete lamellar disruptions are found in the vicinity of defect zones of unordered material (orange ovals in Figure 4F–M). This vicinity is regularly only found if analyzed in 3D, as often the defect zone is some sections away from the lamellar disruption (cf. 4F). In this case, the defect zone extends over 8 sections, corresponding to about 800 nm in Z-direction. Comparing a 3D rendering of the unordered defect (yellow volume in Figure 4P) with its wider surroundings, another type of defect appears (Figure 4Q and Figure S9, Movie S5, Supporting Information). Within the rather ordered zones of neatly stacked lamellae, transition points are found where, for example, fifteen lamellae (8 black/PMMA plus 7 white/PS) are fusing into five (blue oval in Figure 4Q).

To examine which material in these large defect zones prevents the progression of the ordering process at short range and leads to disruptive reorientation of domains again IR-SNOM analysis has been used. Preliminary data show that defect zones consist of a material mix (Figure S8, Supporting Information), which seems not to form the typical lamellar or cylindrical structures found for different phases of block-copolymers. Further characterization of these defects and developing protocols how to manipulate and prevent them need to be investigated in the future.

2.5. Case Study 4 – Opening Up Materials for Analytical TEM: EELS Analysis of Ultrathin Sections of Resin-Embedded Polymeric Microspheres

Ultramicrotomy has long been utilized when TEM analysis of materials was required.[4] Because sample thickness must not exceed a certain value (for carbon materials ≈50–100 nm at 60 keV electron energy – as used in refs.[19,20]) to avoid undesired multiple scattering events within the section, ultramicrotomy is the obvious method of choice. Here, we illustrate an optimized preparation workflow to produce suitable sections for analytical TEM, that is, EELS.

Two species of chemically almost identical polymeric microspheres (a difference of three hydrogen atoms per repeating unit: $C_{20}H_{14}N_2O_6$ versus $C_{20}H_{11}N_2O_6$; for details see Supporting Information and[19]) are not distinguishable by standard SEM or TEM in terms of morphology and conventional amplitude/phase contrast (**Figure 5**A,D). Previous work on mixed carbon systems – such as the bulk heterojunction of organic solar cells – has shown that electron energy loss spectroscopy on thin films in the low energy loss region can be used to obtain material contrast.[20] However, all this work was carried out on thin material films. To investigate the inner chemical materials distribution of 3D microstructures with high spatial resolution it is necessary to initially generate high-quality ultrathin sections. To demonstrate the technique, we prepared sections of simple spherical particles as an example.

Pellets of polymeric microspheres in epoxide resin were produced by centrifugation and cured to harden them for sectioning. Since cutting with a normal diamond knife led to compression artifacts – creating the impression of fused and distorted microspheres (Figure 5B) – we used an oscillating diamond knife. To identify ideal sectioning parameters (see also SI, section 6), many sections were screened. Thus, they were placed on silicon substrates for SEM imaging to allow a higher throughput compared to TEM grids. When sectioned with optimized parameters the individual microspheres appear nicely spaced (Figure 5C). For the final TEM analysis 80 nm thick sections were placed on Quantifoil holey carbon grids, thereby facilitating EEL spectroscopy of free-standing sections (when placed and imaged across the holes). With standard TEM imaging, all microspheres appear to be similar (Figure 5D). In contrast, when an

Table 1. Times needed for sectioning and imaging.

Process			Total time
Automated ultramicrotomy	3 wafers – 19 ribbons 55 sections/ribbon	—	2.5 h
LM → CAT module	1 wafer: Overview, ribbons, 275 or 385 ROIs of 700 × 528 µm at 360 nm pixel size (20× objective)	2.5 h/wafer	7.5 h
SEM → Atlas 5	2 ribbons, selected feature: 110 ROIs of 125.7 × 141 µm at 30 nm pixel size	7 min 18 s /ROI	14 h
Estimated SEM recording time[a)]	1045 ROIs of 700 × 528 µm, at 360 nm pixel size	≈2 min/ROI	35 h

[a)] time to capture SEM images of the 1045 ROIs imaged in the LM with CAT (assuming identical pixel and ROIs sizes).

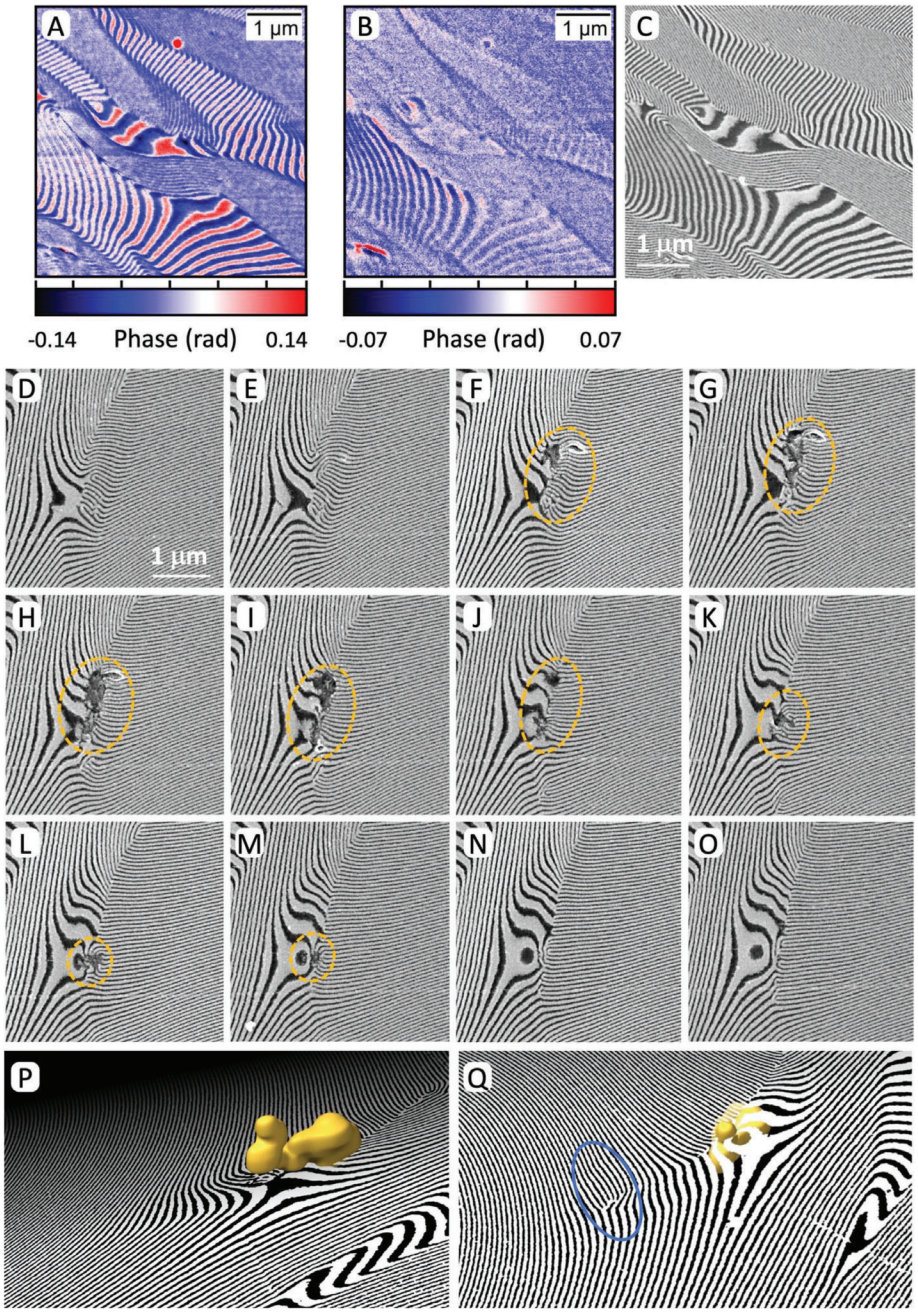

Figure 4. (Case study 3) Analyzing domain boundaries and defects in a block-copolymer. Ultrathin (70 nm) sections of a solvent-annealed PMMA-PS-*block*-copolymer (cf. Supporting Information for further details) on a piece of silicon wafer were analyzed with IR-SNOM: Third-order near-field optical phase images mapped at 1152 (PMMA, A) and 1602 cm^{-1} (PS, B) wavenumber are compared with subsequently acquired SEM data of the identical ROI (C). Serial sections (100 nm in thickness) (D–O) of an embedded PMMA-PS-BCP show a typical defect (orange circles in F–M) extending over 8 sections at a domain boundary. A 3D rendering (yellow feature) of the unordered defect zone (2D views F–M) is displayed in (P), sitting above the last section (cf. E) without visible defect. A "branching" defect within the lamellar zone (blue oval in Q) appears several micrometers away from the unordered defect (cf. Figure S9 and Movie S5, Supporting Information).

image is taken at a characteristic electron energy loss (blue energy range in Figure 5E), two different species appear. In that energy window the EELS signal from one polymeric material (shown in blue) is higher than that from the other (shown in brown) – leading to differential contrast between the two microspheres (Figure 5F).

More information than in a single image is contained in the hyperspectral datasets containing the energy loss signals of interest. Multivariate statistical analysis, that is, machine learning, of hyperspectral EELS datasets overcomes many analytical challenges imposed by noise, which is especially beneficial in the context of beam sensitive soft materials, and has enabled

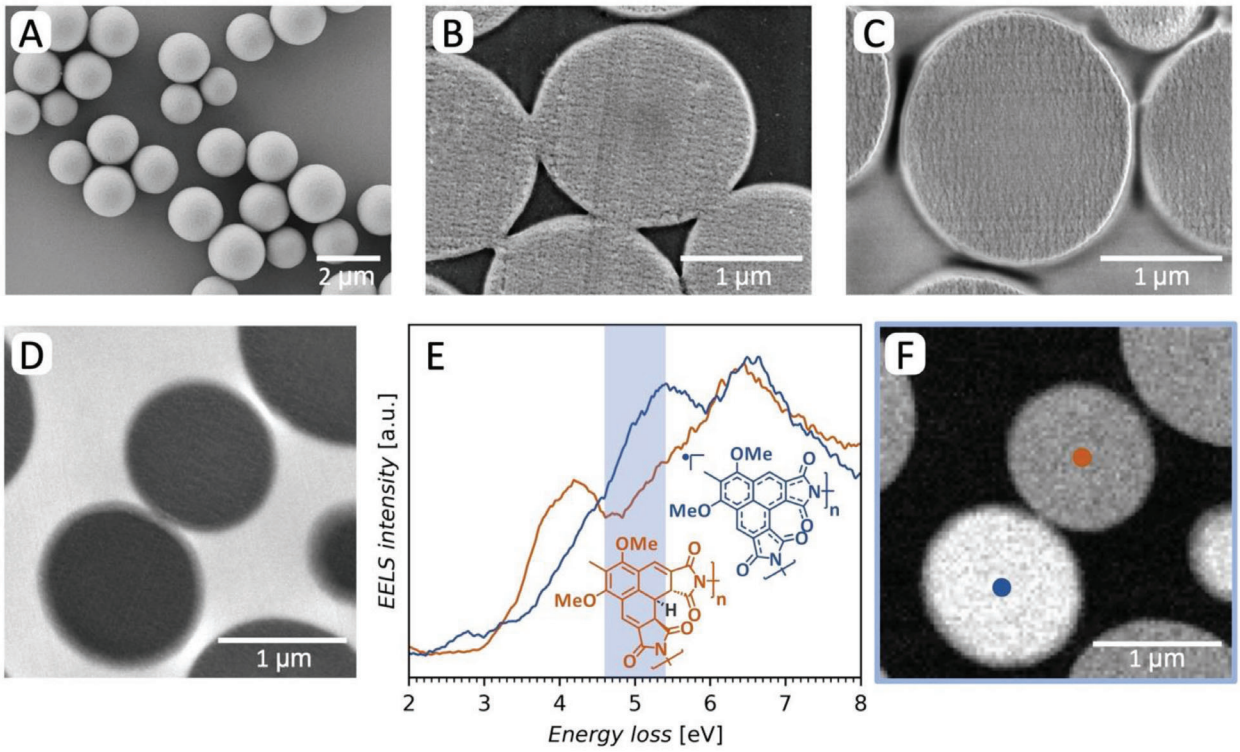

Figure 5. (Case study 4) Opening up materials for analytical TEM. EELS analysis of ultrathin sections of resin-embedded polymeric microspheres. Two species of chemically near identical microspheres with undistinguishable morphology (A) were embedded in epoxide resin and sectioned with an ultrasonic oscillating diamond knife. To optimize the sectioning parameters, sections were first placed on Si wafers pieces and screened in an SEM: bad sectioning without oscillating knife (B), optimized sectioning with oscillating knife (C). Optimal sections on TEM grids were used for TEM analysis: Standard TEM imaging (D) does not allow to distinguish the different carbon materials. Characteristic EELS signals (E) can be utilized to generate contrast between the near identical microspheres, when selecting electrons of an energy loss corresponding to a characteristic EELS signal (blue energy range) for an energy loss specific TEM image (F). The combination of ultramicrotomy and analytical TEM provides nanometer resolved chemical information despite the small chemical difference of only three H atoms in the repeating unit.

improved 3D reconstructions,[21] spectral unmixing,[22] and material classification[23] of low contrast organic heterostructures[20] at high spatial resolution. Herein, we use the combination of dimensionality reduction by Uniform Manifold Approximation and Projection (UMAP)[24] and subsequent agglomerative clustering for material classification in the hyperspectral dataset from 2 to 11 eV energy loss with subsequent quantification of the materials composition by Multivariate Curve Resolution by Log-Likelihood Maximization (MCR-LLM).[25] The dimensionality reduction (**Figure 6**A) reveals four separate clusters, belonging to the two individual functional polymers (species 1 and 2), the embedding resin, and the overlapping areas of functional polymers and embedding resin at the edge of the particles (Figure 6B). We used the averaged spectra of the so obtained clusters as starting points for MCR-LLM, which allowed us to further unmix the spectra (Figure 6C) and obtain the chemical composition with nanometer resolution despite the small chemical difference of the functional polymers of only three hydrogen atoms in the backbone (Figure 6D-F). We refer to section S11, Supporting Information for a detailed discussion and at this point only want to highlight the demonstrated potential of EEL spectroscopy on ultrathin sections – especially when supported by machine learning – for the nano-analysis of low contrast soft materials inside comparably big microstructures.

3. Discussion

New techniques to manufacture complex 3D materials not accessible so far –, for example, in the field of responsive materials[26] and objects consisting of a hybrid mix of carbon materials and biological or biocompatible systems – require novel characterization tools. Here, morphologies bridging length scales (from macro-, micro-, to nanometer scale) and mixed properties of materials lead to new functions in such systems. The correlated characterization of morphology and function – as defined by chemical composition, physical properties, and 3D localization in a complex structure – is crucial.

In this context existing techniques such as non-invasive optical coherence tomography (OCT[27]) or Xray microscopy (XRM) tomography (for its application in materials science see, e.g.,[28]) play an increasing role. In particular, the novel developments of phase contrast XRM have widened the applicability of X-ray tomography. It is presently one of the hot topics in structural cell biology.[29] However, resolution of these non-invasive techniques is limited, and detailed, high-resolution chemical information at the nanometer scale in 3D is simply not achievable so far.[3]

To overcome the limitation of spatial resolution in 3D, invasive techniques such as focused- ion-beam milling[8] as well as plasma[30] and laser milling[31] have been developed and in recent

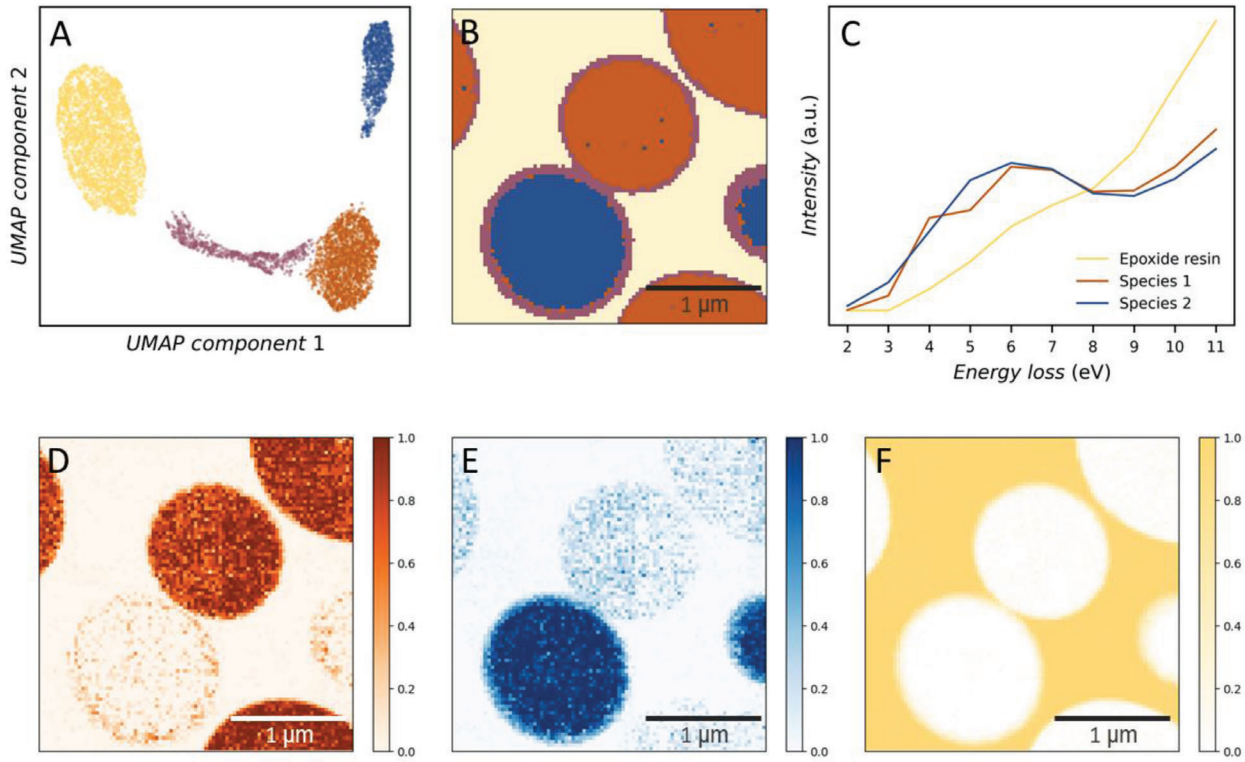

Figure 6. (Case study 4) Machine learning on hyperspectral EELS dataset for quantitative chemical analysis. The dimensionality reduction by UMAP revealed four clusters (A), which allow a material classification (B). The accordingly averaged spectra were used as starting point for MCR-LLM to obtain the unmixed spectra (C) and the corresponding compositional maps of species 1 (D), species 2 (E), and the epoxide resin (F).

years variants of ultramicrotomy sectioning have been advanced for biological samples. There, SBFSEM[6] and AT[9] are well established and used readily in a wide range of applications.[32]

As we illustrate with our four case studies, the modern developments in the field of advanced ultramicrotomy, serial sectioning, and automation of sectioning and imaging can readily be applied to typical carbon materials systems. Here we adapt processes and hard- and software design features from the biomedical research to the specific constraints of materials – as we will discuss in the following.

3.1. Sample Preparation – How to Handle and How to Introduce Contrast without Changing the Materials in a Non-Predictable Manner

Inanimate material samples generally require somewhat different sample preparation methods than conventional biomedical samples. In particular, soft metal samples have been sectioned directly,[4] that is, no special treatment was applied, except for trimming the sample to a small pyramid, which is then sectioned with a diamond knife (cf. SI). In our case study 3, a thick free-standing film of self-organizing block-copolymers could indeed be clamped directly into the ultramicrotome sample holder, allowing for sectioning without any previous preparation (cf. Figure S1, Supporting Information). However, for other samples, an embedding procedure might be necessary. In these cases, a control for changes in morphology is paramount. Thus, either microscopy of unprocessed samples (case study 1) or comparison with direct SEM imaging is advisable (case study 4). Such controls are necessary to exclude obvious morphological changes caused by, for example, solvents of the embedding material or by thermal treatment when curing the embedding resin.

An interesting – even though preliminary – device is illustrated in case study 2. Figure 3A shows our "fork" holding the sample prior to embedding (design and CAD files available from SI). At present, this holding device is passive and a pure geometrical constraint aligning the sample to the later ultra-sectioning axis. One can imagine to extend the functionality of this fork to apply electrical current, temperature changes, or forces to the sample. However, this will require more complex structures, with additional modeling and microengineering steps – which was beyond the scope of our present study. However, the possibility to manipulate the sample prior or during embedding is evident.

Another topic of concern is the necessary contrast of embedded material for high-resolution morphological imaging. In the case of different carbon materials – or biological versus carbon materials in bio-hybrid devices – neither SEM nor TEM imaging will produce sufficient contrast to allow for distinguishing between different materials (cf. case study 4, Figure 5D). If no spectroscopic contrast can be used (see case study 4 and discussion below), staining with metals (preferably high atomic number metals such as U, Os, Pb) is used. For the block-copolymers a RuO_4 vapor stain of the ultrathin sections was used, which covalently binds to benzyl π-electrons.[33] This example illustrates that stains do not necessarily need to be applied in solution, which

again excludes solvents affecting the morphology. Unsaturated carbon bonds, as well as alcohols, amides, and ethers[18] are ideal for binding metals, and future screens for other vapor applicable metals will make this technique more widely applicable. We note that the material films are ultra-thin after sectioning. This helps the metal-oxide vapor to diffuse into the material, which otherwise could only diffuse into a thin skin at the surface of the object.[33]

3.2. Ultra-Sectioning – High-Quality Thinning without Material Dislocation and Beam-Damage Artefacts

Milling and thinning of materials can be done with a variety of standard methods, each of which comes with its own artefacts. However, these artefacts are well studied and can be avoided in some cases. Mechanical or ion milling with, for example, a subsequent polishing with argon ions or argon-clusters, is a common approach. Such polishing is necessary, as milling procedures usually damage the surface of the sample. For polymers this might lead to a quasi-melting when milled with a direct ion beam.[34]

Ultramicrotomy is not free of similar problems, well-known are delamination of multilayer samples, or material dislocation and crevices visible in the surface of the material – as shown for case study 4 in Figure 5B. Similar problems for biological samples have led to the development of oscillating knives. Here, the oscillation of the knife is generated by a piezoelectric actuator. Lateral knife oscillation in the cutting plane can be controlled in amplitude and frequency.[35] By performing cutting tests with the sample optimal amplitude and frequency settings can be identified that minimize or completely eliminate cutting artefacts. In case study 4 crevices are still visible, while material dislocation is no longer observed (cf. Figure 5B,C). Manufacturers of ultramicrotomes specify their instruments down to 20–40 nm section thickness, but typically 60–80 nm can routinely be cut, mainly limited by the mechanical properties of sample and embedding resin.

Another very important development, especially for serial sectioning of large volumes, is fully automated and computer-controlled sectioning. It has been shown that the fabrication of section ribbons can be controlled to produce ribbons with a predefined number of sections. These can then be manipulated as compact unit and placed in surface structured channels on a solid substrate.[14] Figure 3B shows one example. It is obvious that this development is most important for studying large 3D volumes of objects cut open and then imaged by hierarchical AT – as illustrated in case studies 1–3.

3.3. Automation and Correlation of Multimodal Morphological and Analytical Imaging

AT has been introduced here as a method for imaging of a large number of serial sections with different modalities in a hierarchical way.[9,32] As materials scientists we benefit in particular from hardware and software developed for correlating LM and SEM. Recently, such workflows have also been transferred to typical materials science microscopy setups, such that epi-fluorescent images of samples, or epi-dark-field imaging – as in case study 2 – can immediately be used for navigating the section arrays in an SEM (see also Figure S4, Supporting Information). This provides very efficient imaging workflows which allow fast targeting of the most interesting sample areas within the section sets without any previous tomographic bulk analysis as discussed before. This additional step in the analysis workflow can now reasonably well be replaced by automated sectioning and imaging procedures.

Unfortunately, the necessary software is usually bound to commercial imaging platforms of individual manufacturers. The development of cross platform open-source software for correlative imaging is an unavoidable prerequisite to make correlative imaging more accessible and increase the available imaging modes.

Open cross-platform correlative imaging software would also allow a more seamless correlation between AT and analytical TEM. The large specimen chamber of an SEM easily allows mounting of even entire 4-Inch wafers carrying large numbers of sections,[36] whereas TEM substrates are much smaller (grids of 3 mm diameter). The number of sections fitting onto such a substrate is rather limited, making it very tedious to deal with hundreds of sections as, for example, in our case study 2. An analytical inspection of hundreds or even thousands of sections is currently very labor intensive, and any automated correlation would need very extensive new developments. As shown in our case study 4, very important results can also be obtained without any correlated light and electron microscopy.[19]

The situation is different, however, for correlating imaging on section arrays in LM and SEM and possible correlated probe microscopy. In case study 3, we show such a correlation for IR-SNOM-imaging of the block-copolymer sections. This correlation was so far facilitated using fiducials on the samples and simply correlating features of the imaged film. However, it is obvious that an automated correlation workflow can be implemented in the future. As in case study 3 the comparison of spectroscopic and imaging data will help to identify different materials in the SEM even in cases when staining has to be minimized or is not advised at all.

If the unstained materials show distinct EEL spectra, then producing contrast between materials by spectroscopic imaging is a very attractive idea. At present, such materials identification via EELS – as illustrated in case study 4 – is only available from analytical TEMs or few SEMs with special spectrometer attachments operating in transmission mode.[37] The used acceleration voltages – typically 30–300 keV for TEMs and $\lesssim$30 keV for SEMs – restrict the material dependent sample thickness to meet the requirements for electron transparency and the multiplicity of scattering.[38] Here we note that the typical section thickness of 60–100 nm is still thin enough to find acceptable levels of multiple scattering in the low energy loss region of the spectra. If distinct features exist in the range of 2–10 eV loss (optical and UV absorption) then TEM-EELS will provide statistically significant materials segmentation – as illustrated in case study 4. For transmission SEM-EELS the situation is more critical, there much thinner samples are needed and ultra-sectioning appears not to be a suitable sample preparation method.

If EELS would become commonly available in the standard SEM setting operating in non-transmission mode, then sample thickness would no longer matter. Here first results of spectroscopy on secondary electrons and backscattered electrons are

available,[39] which indicate that back-scattered electrons carry the electron energy loss signals for optical and UV excitations (low loss region as discussed above). Materials identification in the SEM could then be done at much lower primary electron energies, which in turn will restrict the signal readout to a very thin layer below the sample surface. This will effectively minimize or even eliminate any spectral mixing from different materials as is seen in the TEM-EELS (cf. Figure 6B, where the rims of the tangentially cut spheres are assigned a "mixed" material ring. SEM-EELS and AT will then be a very attractive technique for large scale materials segmentation without staining.

3.4. Opening New Vistas for Spatially Resolved Spectroscopy in 3D

In general, soft matter materials science aims in many fields for increasingly well-defined micro- and nano-morphologies,[40] reflected in complex self-assemblies, structurally highly optimized devices, polymer networks with spatiotemporal controllable chemistry and properties, as well as in complex post-functionalization. Many of these efforts result in nanopatterned heterostructures, for which the local distribution of the different components or functional groups dictate the material properties. For establishing these structure-property relationships, understanding the formation of the structures, and optimizing the materials, nanometer-resolved spectroscopic information is necessary, which cannot be provided by common spectroscopic methods, such as IR and NMR. We demonstrate this statement in case study 4, where the two differently post-functionalized polymeric microspheres can be discriminated based on characteristic electron energy loss signals despite minimal chemical differences. More importantly, we demonstrate that the post functionalization is homogeneous throughout the whole particle volume. This finding is surprising, given the solid-state post functionalization of two completely insoluble polymers.[19] Thus, the applicability of the material system could be proven, facilitated by the high analytical sensitivity of EELS at nanometer resolution. EELS can not only pick up optical excitations with nanometer resolution, but also the atomic composition from ionization events and with high-end monochromation even IR signals.[41] In a similar manner, SNOM can pick up IR (cf. case study 3), as well as optical signals in the visible range with nanometer resolution.[42] Another method that provides insights into chemical and material distributions with nanometer resolution is super-resolution optical microscopy of fluorescence signals.[43] For all these spectroscopic methods, ultramicrotomy makes the inner chemical and material distribution of large structures accessible, without chemically altering the material during the sample preparation. This aspect is especially important, if a selective staining cannot be achieved, the morphology would be altered in the staining process, or a higher analytical sensitivity is needed.

However, it should be noted, that spatial resolution on the sections (x,y lateral resolution) is as good as contrast of the sample and SEM instrument allows, that is, with a modern field emission instrument in the order of nanometer. Modern instruments can therefore visualize also complex materials distributions, as long as material contrast can be provided. The situation is different in z-direction, where the section thickness defines resolution.

4. Conclusions

The four case studies discussed herein illustrate the range of possibilities for using ultramicrotomy in different fields of morphological characterization of manufactured 3D structured carbon materials. Technical advances such as oscillating diamond knives and computer-controlled ultra-sectioning have allowed to find cutting parameters minimizing sectioning artefacts – at least for most carbon materials and resin embedded samples. As we have shown, it is feasible to produce high-quality ultrathin sections in large numbers, making it possible to access samples' 3D information by serial sectioning and imaging.

Physically slicing a larger 3D structure with an ultramicrotome is no longer a tedious task but can be achieved within hours, including targeting for a predefined volume of interest. In the future, such targeting will ideally be conducted before sectioning by XRM, an approach that has been described already in different biological[44] and materials systems.[45] However, automation of sectioning and imaging allow an efficient and targeted analysis even without prescreening. In addition, depending on the sample, imaging contrast – and thus information about the object – may only be obtained after sectioning and prescreening may therefore be precluded. The lack of pre-sectioning targeting appears not to be a problem when utilizing AT, as even a large number of serial sections can be imaged in a hierarchical manner and targeting on the sections from the macro- to micro- to nano-scale is readily possible.

Furthermore, we have illustrated that correlation of different imaging instruments, such as light microscopes (incl. epi- and fluorescent modalities), electron microscopes, and probe microscopes allow for a seamless combination of different imaging and spectroscopy data across scales and physical properties. It is important to note that the case studies indicate an obvious roadmap for combining morphology with materials properties from 2D to 3D.

Imaging, using automated AT and spectroscopic imaging modalities can provide quantitative data: Statistical analysis of properties that can be visualized – such as porosity, morphology, materials distributions – can now be performed in large volumes. The obvious "randomness" when looking only at a small selection of sample areas can thus be avoided. Therefore, serial ultramicrotomy in its modern, scale- and modality crossing realization provides a powerful toolbox for a comprehensive characterization of complex structured carbon materials.

5. Experimental Section

Refer to Supporting Information section for experimental details.

Supporting Information

Supporting Information is available from the Wiley Online Library or from the author.

Acknowledgements

I.W., R.C., D.R., and R.R.S. acknowledge key funding for these case studies and the ultramicrotomy project by the Deutsche Forschungsgemeinschaft

(DFG, German Research Foundation) under Germany's Excellence Strategy for the Excellence Cluster "3D Matter Made to Order" (EXC-2082/1 – 390761711). B.W., F.M., M.I., N.vC., T.H., C.H., P.T., F.F., J.A.K., C.B.-K., M.W., and E.B. likewise acknowledge funding by the Deutsche Forschungsgemeinschaft (DFG, German Research Foundation) under Germany's Excellence Strategy for the Excellence Cluster "3D Matter Made to Order" (EXC-2082/1 – 390761711) for the individual projects described here as part of the case studies. B.W. and T.S. thank the Carl Zeiss Foundation for financial support. J.A.K is currently supported by the Deutsche Forschungsgemeinschaft (DFG, German Research Foundation) with a WBP fellowship – 500289223. C.B.-K. additionally acknowledges continued support by the Australian Research Council (ARC) in the context of a Laureate Fellowship, as well as continued support by QUT's Centre for Materials Science. I.W., R.C., and R.R.S. also acknowledge funding by the German Ministry for Research and Education under the Project "NanoPatho," FKZ 14N14476, as well as support by the University Computing Centre of the University Heidelberg regarding Research Data Management/ELN and the data storage service SDS@hd supported by the Ministry of Science, Research and the Arts Baden-Württemberg (MWK) and the German Research Foundation (DFG) through grant INST 35/1314-1 FUGG and INST 35/1503-1 FUGG. L.-Y.H., J.H., and U.G. acknowledge funding by the program Material Systems Engineering of the Helmholtz Association

Open access funding enabled and organized by Projekt DEAL.

Conflict of Interest

The authors declare no conflict of interest.

Author Contributions

The experimental ultramicrotomy part of the study and the examples was shared by I.W., R.C., D.R., B.W., and J.A.K. The automation of ultrasectioning was developed and provided to the project by J.H., L.-Y.H and U.G. SEM and Light microscopy imaging was shared by I.W., R.C., D.R., and B.W.; analytical TEM was performed by J.A.K. and D.R., EELS data analysis by J.A.K, SNOM probe microscopy by N.v.C., T.S., and C.H. Samples for the case studies were provided by F.M. (case study 1), M.I. and L.-Y.H. (case study 2), B.W. (case study 3) and F.F. (case study 4). Visualization in 3D and movies by R.R.S. The project leaders M.W., P.T., C.B.K., E.B. and R.R.S. of the Cluster of Excellence '3DMM2O' developed materials and concepts and posed the challenges leading to this study. I.W. and R.R.S. put together the draft and all authors reviewed and edited the manuscript. All authors were involved in the final interpretation of the results.

Data Availability Statement

The data that support the findings of this study are available in heiDATA at https://doi.org/10.11588/data/TOEQZB.

Keywords

3D microscopy, array tomography, correlative light and electron microscopy, probe microscopy, spectroscopy, structured materials, ultramicrotomy

Received: February 21, 2023
Revised: May 29, 2023
Published online: July 8, 2023

[1] M. Kadic, G. W. Milton, M. van Hecke, M. Wegener, *Nat. Rev. Phys.* **2019**, *1*, 198.
[2] a) V. Hahn, T. Messer, N. M. Bojanowski, E. R. Curticean, I. Wacker, R. R. Schröder, E. Blasco, M. Wegener, *Nat. Photonics* **2021**, *15*, 932; b) F. Mayer, D. Ryklin, I. Wacker, R. Curticean, M. Calkovský, A. Niemeyer, Z. Dong, P. A. Levkin, D. Gerthsen, R. R. Schröder, M. Wegener, *Adv. Mater.* **2020**, *32*, 2002044.
[3] F. Lutter, P. Stahlhut, K. Dremel, S. Zabler, J. Fell, H.-G. Herrmann, R. Hanke, *Nucl. Instrum. Methods Phys. Res. B* **2021**, *500–501*, 10.
[4] a) T. F. Malis, D. Steele, *MRS Online Proc. Lib.* **1990**, *199*, 3; b) G. Mc Mahon, T. Malis, *Microsc. Res Tech* **1995**, *31*, 267. c) T. R. Guimaraes, M. Kahn, R. P. Kuchel, J. C. Morrow, H. Minami, G. Moad, S. Perrier, P. B. Zetterlund, *Macromolecules* **2019**, *52*, 2965.
[5] I. Wacker, E. Hummel, S. Burgold, R. Schröder, *Volume Microscopy, Multiscale Imaging with Photons, Electrons, and Ions*, Humana Press, New York, USA **2020**.
[6] W. Denk, H. Horstmann, *PLoS Biol.* **2004**, *2*, e329.
[7] T. Hashimoto, G. E. Thompson, X. Zhou, P. J. Withers, *Ultramicroscopy* **2016**, *163*, 6.
[8] A. Zankel, J. Wagner, P. Poelt, *Micron* **2014**, *62*, 66.
[9] I. Wacker, R. R. Schröder, *J. Microsc.* **2013**, *252*, 93.
[10] M. Calkovský, E. Müller, M. Meffert, N. Firman, F. Mayer, M. Wegener, D. Gerthsen, *Mater. Charact.* **2021**, *171*, 110806.
[11] C. S. Xu, S. Pang, K. J. Hayworth, H. F. Hess, in *Volume Microscopy* (Eds: I. Wacker, E. Hummel, S. Burgold, R. Schröder), Humana Press, New York, USA **2020**, *155*.
[12] J. Bauer, A. Schroer, R. Schwaiger, O. Kraft, *Nat. Mater.* **2016**, *15*, 438.
[13] M. Islam, J. Flach, R. Martinez-Duarte, *Carbon* **2018**, *133*, 140.
[14] a) J. Hoffmann, S. M. Gamboa, A. Hofmann, H. Gliemann, A. Welle, I. Wacker, R. R. Schröder, L. Ness, V. Hagenmeyer, U. Gengenbach, *Sci. Rep.* **2019**, *9*, 17952; b) J. Hoffmann, V. Hagenmeyer, R. R. Schröder, Automation of section acquisition for Array Tomography, Thesis Dr.-Ing KIT, Karlsruhe, Germany **2023**.
[15] a) A. Cardona, S. Saalfeld, J. Schindelin, I. Arganda-Carreras, S. Preibisch, M. Longair, P. Tomancak, V. Hartenstein, R. J. Douglas, *PLoS One* **2012**, *7*, e38011; b) J. Schindelin, I. Arganda-Carreras, E. Frise, V. Kaynig, M. Longair, T. Pietzsch, S. Preibisch, C. Rueden, S. Saalfeld, B. Schmid, J.-Y. Tinevez, D. J. White, V. Hartenstein, K. Eliceiri, P. Tomancak, A. Cardona, *Nat. Methods* **2012**, *9*, 676.
[16] E. F. Pettersen, T. D. Goddard, C. C. Huang, G. S. Couch, D. M. Greenblatt DM, E. C. Meng, T. E. Ferrin, *J. Comput. Chem.* **2004**, *25*, 1605.
[17] a) F. S. Bates, G. H. Fredrickson, *Phys. Today* **1999**, *52*, 32; b) C. Park, J. Yoon, E. L. Thomas, *Polymer* **2003**, *44*, 6725; c) I. W. Hamley, *Nanotechnology* **2003**, *14*, R39; d) T. Smart, T. Lomas, M. Massignani, M. V. Flores-Merino, L. Ruiz-Perez, G. Battaglia, *Nano Today* **2008**, *3*, 38; e) J. K. Kim, S. Y. Yang, Y. Lee, Y. Kim, *Prog. Polym. Sci.* **2010**, *35*, 1325.
[18] J. S. Trent, J. I. Scheinbeim, P. R. Couchman, *Macromolecules* **1983**, *16*, 589.
[19] J. A. Kammerer, F. Feist, D. Ryklin, A. Sarkar, C. Barner-Kowollik, R. R. Schröder, *Adv. Mater.* **2023**, *35*, 2211074.
[20] a) M. Pfannmöller, H. Flügge, G. Benner, I. Wacker, C. Sommer, M. Hanselmann, S. Schmale, H. Schmidt, F. A. Hamprecht, T. Rabe, W. Kowalsky, R. R. Schröder, *Nano Lett.* **2011**, *11*, 3099; b) W. Köntges, P. Perkhun, J. Kammerer, R. Alkarsifi, U. Würfel, O. Margeat, C. Videlot-Ackermann, J. Simon, R. R. Schröder, J. Ackermann, M. Pfannmöller, *Energy Environ. Sci.* **2020**, *13*, 1259.
[21] O. Nicoletti, F. de la Pena, R. K. Leary, D. J. Holland, C. Ducati, P. A. Midgley, *Nature* **2013**, *502*, 80.
[22] F. de la Peña, M.-H. Berger, J.-F. Hochepied, F. Dynys, O. Stephan, M. Walls, *Ultramicroscopy* **2011**, *111*, 169.
[23] P. Torruella, M. Estrader, Al. López-Ortega, M. D. Baró, M. Varela, F. Peiró, S. Estradé, *Ultramicroscopy* **2018**, *185*, 42.
[24] L. McInnes, J. Healy, J. Melville, **2020** arXiv:1802.03426v3 [stat.ML].
[25] F. B. Lavoie, N. Braidy, R. Gosselin, *Chemom. Intell. Lab. Syst.* **2016**, *153*, 40.

[26] C. A. Spiegel, M. Hippler, A. Münchinger, M. Bastmeyer, C. Barner-Kowollik, M. Wegener, E. Blasco, *Adv. Funct. Mater.* **2020**, *30*, 1907615.
[27] a) D. Huang, E. A. Swanson, C. P. Lin, J. S. Schuman, W. G. Stinson, W. Chang, M. R. Hee, T. Flotte, K. Gregory, C. A. Puliafito, J. G. Fujimoto, *Science* **1991**, *254*, 1178. b) J. G. Fujimoto, Co. Pitris, S. A. Boppart, M. E. Brezinskiz, *Neoplasia* **2000**, *2*, 9.
[28] L. Zhang, S. Wang, *Materials* **2018**, *11*, 1795.
[29] P. O. Bayguinov, M. R. Fisher, J. A. J. Fitzpatrick, *J. Biol. Chem.* **2020**, *295*, 15782.
[30] a) S. Vitale, J. D. Sugar, *Microsc. Microanal* **2022**, *28*, 646; b) T. L. Burnett, R. Kelley, B. Winiarski, L. Contreras, M. Daly, A. Gholinia, M. G. Burke, P. J. Withers, *Ultramicroscopy* **2016**, *161*, 119.
[31] B. Tordoff, C. Hartfield, A. J. Holwell, S. Hiller, M. Kaestner, S. Kelly, J. Le, S. Müller, F. Perez-Willard, T. Volkenandt, R. White, T. Rodgers, *Appl. Microsc.* **2020**, *50*, 24.
[32] a) I. Wacker, W. Spomer, A. Hofmann, M. Thaler, S. Hillmer, U. Gengenbach, R. R. Schröder, *BMC Cell Biol.* **2016**, *17*, 38; b) I. U. Wacker, L. Veith, W. Spomer, A. Hofmann, M. Thaler, S. Hillmer, U. Gengenbach, R. R. Schröder, *J. Vis. Exp.* **2018**, *133*, e57059,.
[33] T. M. Chou, P. Prayoonthong, A. Aitouchen, M. Libera, *Polymer* **2002**, *43*, 2085.
[34] a) N. D. Bassim, B. T. De Gregorio, A. L. D. Kilcoyne, K. Scott, T. Chou, S. Wirick, G. Cody, R. M. Stroud, *J. Microsc.* **2012**, *245*, 288; b) S. Kim, M. J. Park, N. P. Balsara, G. Liu, A. M. Minor, *Ultramicroscopy* **2011**, *111*, 191.
[35] D. Studer, H. Gnägi, *J. Microsc.* **2000**, *197*, 94.
[36] Y. Sun, C. Thomas, T. Mikuni, D. Guerrero-Given, R. Yasuda, N. Kamasawa, in *Volume Microscopy* (Eds: I. Wacker, E. Hummel, S. Burgold, R. Schröder), Humana Press, New York, USA **2020**
[37] A. Khursheed, N. Karuppiah, M. Osterberg, J. T. L. Thong, *Rev. Sci. Instrum.* **2003**, *74*, 134.
[38] R. F. Egerton, *Phys. Status Solidi A* **1976**, *37*, 663.
[39] R. R. Schröder, B. Schindler, M. Schnell, C. Hendrich, J. Wensorra, W. Zhang, J. Eisele, L. Veith, J. Kammerer, M. Pfannmöller, D. Preikszas, I. Wacker, *Microsc. Microanal.* **2018**, *24*, 626.
[40] a) A. S. Abd-El-Aziz, M. Antonietti, C. Barner-Kowollik, W. H. Binder, A. Böker, C. Boyer, M. R. Buchmeiser, S. Z. D. Cheng, F. D'Agosto, G. Floudas, H. Frey, G. Galli, J. Genzer, L. Hartmann, R. Hoogenboom, T. Ishizone, D. L. Kaplan, M. Leclerc, A. Lendlein, B. Liu, T. E. Long, S. Ludwigs, J.-F. Lutz, K. Matyjaszewski, M. A. R. Meier, K. Müllen, M. Müllner, B. Rieger, T. P. Russell, D. A. Savin, et al., *Macromol. Chem. Phys.* **2020**, *221*, 2000216; b) S. P. O. Danielsen, H. K. Beech, S. Wang, B. M. El-Zaatari, X. Wang, Sapir, T. O., Z. Wang, P. N. Johnson, Y. Hu, D. J. Lundberg, G. Stoychev, S. L. Craig, J. A. Johnson, J. A. Kalow, B. D. Olsen, M. Rubinstein, *Chem. Rev.* **2021**, *121*, 5042; c) R.-Y. Wang, M. J. Park, *Ann. Rev. Mater. Res.* **2020**, *50*, 521.
[41] J. A. Hachtel, J. Huang, I. Popovs, S. Jansone-Popova, J. K. Keum, J. Jakowski, T. C. Lovejoy, N. Dellby, O. L. Krivanek, J. C. Idrobo, *Science* **2019**, *363*, 525.
[42] A. Jarzembski, C. Shaskey, K. Park, *Front. Energy* **2018**, *12*, 43.
[43] D. V. Chapman, H. Du, W. Y. Lee, U. B. Wiesner, *Prog. Polym. Sci.* **2020**, *111*, 101312.
[44] E. A. Bushong, S. Phan, M. H. Ellisman, in *Volume Microscopy, Springer Neuromethods* (Eds: I. Wacker, E. Hummel, S. Burgold, R. Schröder), Humana Press, New York, USA **2020**.
[45] P. M. Sarosi, J. Furmanski, W. C. Reese, D. L. Carpenter, M. A. Nittoli, M. G. Myers, N. M. Callen, T. Neeraj, *Sci. Adv.* **2022**, *8*, eabj6738.

ADVANCED FUNCTIONAL MATERIALS

Supporting Information

for *Adv. Funct. Mater.*, DOI 10.1002/adfm.202302025

Deconstructing 3D Structured Materials by Modern Ultramicrotomy for Multimodal Imaging and Volume Analysis across Length Scales

Irene Wacker, Ronald Curticean, Daniel Ryklin, Britta Weidinger, Frederik Mayer, Li-Yu Huang, Julian Hoffmann, Monsur Islam, Nadine von Coelln, Tanja Schmitt, Christian Huck, Petra Tegeder, Florian Feist, Jochen A. Kammerer, Christopher Barner-Kowollik, Martin Wegener, Eva Blasco, Ulrich Gengenbach and Rasmus R. Schröder**

Supporting Information

Modern ultramicrotomy facilitates multimodal imaging and volume analysis of 3D structured materials across length scales

Irene Wacker, Ronald Curticean, Daniel Ryklin, Britta Weidinger, Frederik Mayer, Li-Yu Huang, Julian Hoffmann, Monsur Islam, Nadine von Coelln, Tanja Schmitt, Christian Huck, Petra Tegeder, Florian Feist, Jochen Kammerer, Christopher Barner-Kowollik, Martin Wegener, Eva Blasco, Ulrich Gengenbach, Rasmus R. Schröder**

The research data supporting this publication can be accessed at doi:

heiData and heiArchive; will be activated when paper is accepted

Contents

1. Materials

All materials were reagent grade and used as received, unless stated otherwise.
Dichloromethane, chloroform, ethanol, methanol, ethanol dried - max. 0.01 % H_2O, acetone dried - max. 0.0075 % H_2O (both SeccoSolv).
Monomers case study 1: Pentaerythritol triacrylate (PETA, Sigma-Aldrich), irgacure 819 (Sigma-Aldrich), 2,2,6,6-tetramethylpiperidinyloxyl (TEMPO, Sigma-Aldrich), dodecyl acetate (Sigma-Aldrich), and octadecyl acetate (TCI Chemicals)
Monomers case study 3: Hydroxyethyl methacrylate (HEMA), Methyl methacrylate (MMA) and styrene (Sigma-Aldrich) were purified over Al_2O_3 (basic, Honeywell) to remove the respective inhibitor and stored at -18 °C. CuBr (Sigma Aldrich) was transferred to and stored in a dry box and small amounts were removed and used over the course of a few days. Ethyl-α–bromoisobutyrate and N,N,N′,N″,N″-Pentamethyldiethylentriamin (PMDETA, Sigma Aldrich) were used as received. Unless denoted otherwise, solvents were technical grade quality.
0.5 % RuO_4 solution in H_2O (Polysciences) (quenched in 10 % aq. $Na_2S_2O_5$ after use)
OsO_4 crystals, 250 mg pre-weighed in glass ampoules (Electron Microscopy Services)
EPON (all components from Serva): glycid ether 100, dodecenylsuccinic acid anhydride, methyl-5-norbornene-2,3-dicarboxylic anhydride, benzyldimethylamine
Spurr (all components from Sigma Aldrich): 3,4-Epoxycyclohexanemethyl 3,4-epoxycyclo-hexanecarboxylate **(**ERL 4221**),** Diglycidyl ether of polypropylene glycol (D.E.R. 736), Nonenyl succinic anhydride (NSA,) Dimethylaminoethanol (DMAE).

2. Instrumentation

Laser microprinting: On a commercial instrument (Photonic Professional GT, Nanoscribe GmbH, Germany) a 25×/NA 0.8 objective lens (Zeiss LCI Plan-Neofluar 25×/0.8) was used in dip-in mode. Printing parameters were: focus velocity 5 cm s^{-1}, slicing distance 1 µm, and hatching distance 0.5 µm. A silicone chamber, connecting objective lens and sample holder, was fed with a constant flow of nitrogen during printing.

Ultramicrotome: Ultra-thin sections were cut with a PowerTome PC ultramicrotome (RMC Boeckeler, Tucson, USA).

Light microscopy (LM): An upright light microscope (AxioImager 2, Carl Zeiss Microscopy, Oberkochen, Germany) with long distance objectives, a motorized stage and ZEN software with the "tiles module" for creating large area mosaics was used for standard imaging. Automated imaging of large numbers of sections (>1000) was done in a hierarchical manner, assisted by the correlative array tomography (CAT) module: On a large area mosaic (e.g., an entire 22 × 22mm piece of silicon wafer with several hundred sections) the individual ribbons are outlined manually and recorded. Then individual sections, recognized, outlined and numbered by the software, can be recorded in a fully automated way, creating ordered image stacks.

Scanning Electron Microscopy (SEM): A field-emission SEM, Ultra 55 (Carl Zeiss Microscopy, Oberkochen, Germany) was operated at 1.5 keV primary electron energy and 43 pA beam current (20μm aperture) for imaging with either the chamber SE2 (Everhart–Thornley) detector, the In-lens SE detector, or the energy-selective backscattered electron (ESB) detector, or, in some cases, by simultaneous imaging with any two of those.
Automated recording of large fields of view and/or stacks of serial sections using an external scan generator (up to 32000 × 32000 pixels) was done with the Atlas 5 software (Carl Zeiss Microscopy, Oberkochen, Germany), see also below, section 7.

Transmission Electron Microscopy (TEM): A Libra 200 MC (Carl Zeiss Microscopy, Oberkochen, Germany), equipped with a monochromator, spherical aberration correction and a corrected omega in-column filter[1], was operated at 60 keV for performing electron energy loss spectroscopy (EELS) and electron spectroscopic imaging (ESI) with a Köhler illumination setup with parallel beam. For EELS, a monochromator slit of 0.5 μm was used, for ESI a monochromator slit of 2 μm, resulting in a dose rate of 30 e nm^{-2} s^{-1} and 73 e nm^{-2} s^{-1}, respectively. For EELS and ESI, an angle limiting objective aperture was used with an acceptance angle of at 1.7mrad, corresponding to a maximum scattering vector of 0.7 nm^{-1}. For each EEL spectrum, a total dose of 144 e nm^{-2} was accumulated over several spectra shifted by 0.5 eV on the camera by increasing the acceleration voltage to decrease static noise. The spectra of the microspheres were acquired with a spectrometer entrance aperture with a virtual diameter of 350 nm in the respective image plane. ESI was performed with an energy selective slit of 0.7 eV width. The hyperspectral ESI data set was recorded from 2 to 40 eV with an increment of 1 eV. The hyperspectral dataset was normalized pixel-wise by the integral from 10 to 40 eV (volume plasmon) to minimize thickness influences. Each ESI image accumulated a dose of 146 e nm^{-2}.

Probe microscopy: Infrared-scanning near-field microscopy (IR-SNOM) was carried out using a commercially available setup (neaSNOM, Neaspec, München, Germany). Topography, optical amplitude and phase maps (5 × 5 μm^2, 500 × 500 pixels, 6.6 ms integration time) were recorded simultaneously by operating the system in tapping mode employing a pseudo-heterodyne detection scheme.[3] A platinum-iridium coated probe (Arrow-NCPt) with a resonance frequency of 269 kHz was used and illuminated with a mid-infrared quantum cascade laser (Daylight solutions, San Diego, USA) tuned to a wavenumber of 1152 cm^{-1} or 1602 cm^{-1}. The signal, which was detected with a mercury cadmium telluride (MCT) detector, was demodulated at the third harmonic of the tapping frequency to suppress the background signal.

3. Fabrication of samples

Porous polymer pillars (case study 1) were printed from a photoresist mixture consisting of PETA (52.94 %), irgacure 819 (2.12 %,), TEMPO, (0.0 7%), dodecyl acetate (22.43 %), and octadecyl acetate (22.43 %). Samples were developed in acetone and critical point dried in a commercial instrument (Leica EM CPD 300). For further details see[2b – main text].

Pyrolized paper origami (case study 2): A cellulose sheet (Whatman filter paper Grade 1) was pre-creased using a CO_2 laser engraving machine, manually folded into a precursor origami, heated to 900 °C in a tube furnace (Carbolite Gero, Neuhausen, Germany) at 5 °C min^{-1} and kept for 1 h at 900 °C, all heating under constant nitrogen flow.[13 – main text]
PS-P(MMA-co-HEMA) block-copolymer film (case study 3): PS-P(MMA-co-HEMA) was synthesized by polymerizing styrene using ATRP with CuBr as catalyst, PMDETA as ligand and ethyl-α–bromoisobutyrate as initiator in a ratio of sty:Cu:L:I = 1300:1:1:1 at 110 °C for 7 h under argon atmosphere. After filtration over Al2O3 and precipitation in MeOH, the received macroinitiator PS-Br (M_n = 29 kDa) was chain extended with MMA:HEMA:Cu:PMDETA:PS-Br = 1200:338:1:1:1 at 100 °C for 2 h under argon atmosphere. Block copolymer PS-*b*-(MMA-*co*-HEMA) (M_n = 62 kDa) was obtained after filtration and precipitation. To introduce self-assembly by solvent-annealing, a 5 % block copolymer solution in chloroform was slowly evaporated from a saturated chloroform atmosphere over the course of several days in a desiccator, yielding a film which is free standing after removal from the vial.

Polymer microspheres (case study 4) were synthesized by precipitation photopolymerization and further modified in solid state (for more details [19] main text). For size determination in the SEM, dry microspheres were dispersed in acetone and drop cast onto a piece of silicon wafer. Dried samples were sputter coated in a QV 150 ES plus (Quorum Technologies, Laughton, UK) with 3 to 6 nm of Pt/Pd 80/20.

4. Staining

Pre-embedding stain: Pre-weighed OsO_4 crystals were dissolved in dry acetone to 2 % (wt/vol) and transferred to a weighing glass with tight lid. Porous polymer pillars were submerged in the liquid and incubated for 24 h.

Vapour staining of sections: A ready-made solution of RuO_4 in water was placed into an open 35mm diameter glass Petri dish. Pieces of silicon wafer with ultrathin sections of the block.copolymer film-film, sitting on the inverted lid of the Petri dish were placed close to the solution. Both glass dishes were covered with a large glass Petri dish and incubated for 30 min.

5. Embedding

Epon (42.4 g glycid ether 100, 29.6 g dodecenylsuccinic acid anhydride, 18.4 g methyl-5-norbornene-2,3-dicarboxylic anhydride and 2.4 g benzyldimethylamine as initiator) was used for the porous polymer pillars (case study 1) and the microspheres (case study 4). For the porous pillars, 3h infiltration with a mixture of 50 % Epon in acetone was necessary to

guarantee homogeneous penetration of the embedding resin into the porous sample. Before curing for 2d at 60° (laboratory oven, Memmert, Germany) the sample was transferred to an embedding mold filled with 100 % Epon.
The microspheres were mixed with 100 % Epon in a 200 µL centrifuge tube, sonicated in a water bath for 1 h, centrifuged 5-10 min at 21900 × g to create a pellet, and cured 24 h at 60° C.

Spurr's low viscosity resin, firm (mix 4.10 g ERL 4221, 1.43 g D.E.R. 736, 5.90 g NSA, then add 0.1 g DMAE and mix thoroughly) was used for direct embedding of small pieces of pyrolized paper origami and BCP-films to be used for serial sectioning. Although the BCP-film was in principle thick enough to be clamped into an ultramicrotome sample holder, it had a very irregular shape (cf. figure S1 H) which would have prevented ribbon formation and thus serial sectioning (see below, chapter 6 ultramicrotomy).
BCP film was cut into strips (1 mm × 5-10 mm, figure S1B) and oriented in the embedding mold with the help of a 3D-printed fork (fabricated by fused deposition modeling). This fork prevents the sample from floating freely in the resin and keeps it in an oriented position such that later trimming effort is reduced and serial sectioning is along a main axis of the object. Spurr's resin was placed onto that assembly and the entire mold kept overnight in a sealed box at room temperature before curing for 65 h at 70° C. Similarly, elongated pieces were cut from pyrolized paper origami and embedded accordingly (cf. figure 3A main text).

6. Ultramicrotomy

Trimming: Since the cutting edge of a diamond knife has a width of 3 mm at most and for technical reasons, not more than one third of that should be used for sectioning, samples embedded in resin must be trimmed, meaning superfluous resin has to be removed. The size of the block-face that is being hit by the knife edge (**Figure S1**) should not exceed 1 x 1 mm. For single sections, the shape of the block-face is not critical. To obtain serial sections, sections must adhere to each other and form ribbons that can be manipulated easily. Ribbon formation is only possible when block-faces with exactly parallel leading and trailing edges are trimmed (figure S1 G and FI. Applying glue to the sides of the sample block can help to stabilize ribbons.[32 - main text]

Conventional sectioning: Diamond knives type Ultra (Diatome, Switzerland) with 35° or 45° cutting angle were used for single sections. The cutting speed was typically 1 mm s^{-1}. The water in the knife boat which leads the sections away from the knife edge needs to be ultra-pure (e.g., aqua injectabilia from Braun, Germany or any 'water for injection' from medical suppliers).

Ultrasonic sectioning (case study 4): An oscillating diamond knife (Diatome, Switzerland) with a cutting angle of 35º was used to section the pellets of embedded microspheres. Parameters that were optimized included cutting speed (0.4 and 0.6 mms^{-1}), as well as frequency (20, 25.5, 30, 37.5 and 45 Hz,), and amplitude (1.9, 3.5, 5, 10 and 25 V) of the oscillations. The best combination to obtain 80 nm thick sections without major artifacts (cf. figures 5A and B, main text) was 0.6 mm s^{-1}, 37.5 Hz, and 1.9 V.

Serial sectioning (case study 1): For a small number of serial sections (<100), it is possible to deposit section ribbons onto pieces of silicon wafer manually. To support the operator, we developed a micromanipulator assembly called “advanced substrate holder” or “third hand”. [32 - main text] In that case, even slightly imperfect trimming, leading to curved ribbons, is acceptable, because the ribbons are attached to the silicon substrate by hand before the substrate is gently lifted out of the knife boat using the micromanipulators.

Serial sectioning fully automated (case study 2): The 1045 serial sections (200 nm thick) produced for case study 2 were collected in a fully automated manner, using a custom-made diamond knife (Diatome, Switzerland) and specially pre-treated silicon substrates. [14] - main text] Since the ribbons are being fed into narrow hydrophilic channels on a silanized silicon substrate, exactly parallel trimming is paramount (figure S1I, cf. figure 3B main text).

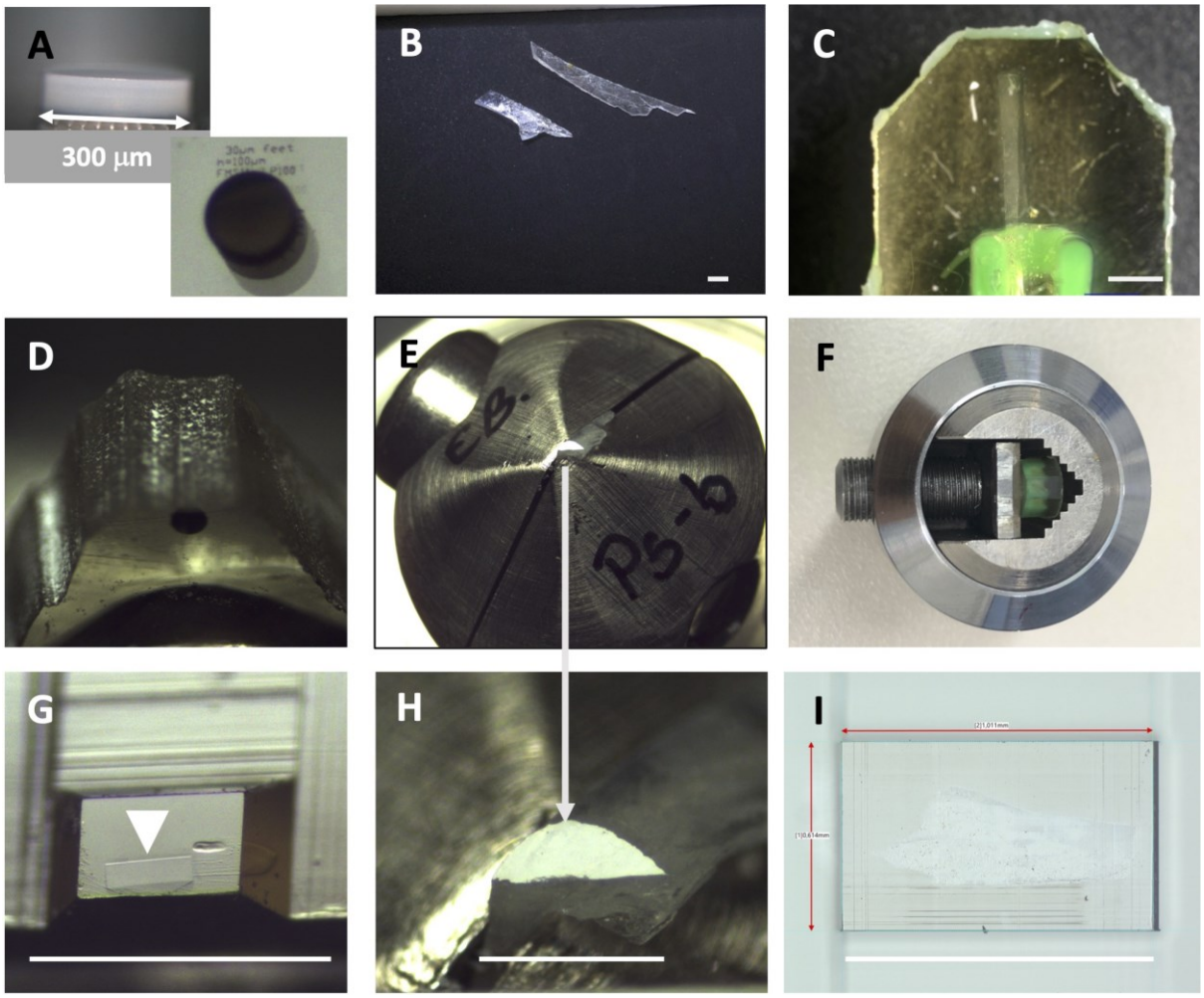

Figure S1. Embedding and trimming: A) polymer cylinder before (A top) and after staining (A bottom) embedded in Epon (D) and after removal of superfluous resin by trimming (G) where the block-face is exposed and shows the cross section of the polymer cylinder (arrowhead). Block-copolymer film (B) clamped into a flat specimen holder (E). To ensure tight gripping of the clamp’s two jaws the sample has to be at least 10 mm long and 0.2 mm thick. The higher magnification in (H) shows the irregular shape of the block face. Embedded piece from the same film (C) in a regular specimen holder before (F) and after trimming for automated serial sectioning (I). All scale bars 1mm.

7. Hierarchical and automated SEM imaging

The Atlas 5 AT module consists of software for navigation and automated recording plus hardware in the shape of an external scan generator that is able to record scan fields of up to 32000 × 32000 pixel. Hierarchical imaging allows time-efficient characterization of large sample areas by recording regions of interest (ROIs) at different positions with different magnifications, applying different imaging parameters. Usually, an overview at low magnification (e.g., 500× = 586 nm pixel size) is recorded first, to map the entire sample. Then, ROIs are placed on prominent features, e.g., sections when serial section imaging is required, and imaged with intermediate magnification (e.g., 6000× = 49 nm pixel size). Finally, based on the information gathered in that imaging round, more ROIs are placed, e.g. at a specific feature within each section, and imaged with high magnification (e.g. 58000× = 5 nm pixel size). During that process the software keeps the positional information of the recorded images and displays each image within the context of the entire sample (cf. **figure S3** and movie 1).
For correlated imaging, it is possible to import images created with other microscopes (e.g. LM in case study 2, see also **figure S4**) and use them as overview image, thus saving the time required to record that image in the SEM (and possibly gaining information not visible in the SEM, such as color). The coordinate system of the LM is transformed into the stage coordinates of the SEM by a three-point alignment procedure (detailed information see [4]).

8. Additional information case study 1

To validate our sample preparation process and check for possible preparation-induced artifacts, especially regarding the porosity of the fabricated polymer pillars, we compared their porosity in native, stained and embedded state. Untreated pillars or pillars air-dried after staining with OsO_4 were cut in two halves with a scalpel, glued onto a sample holder fracture face up and imaged in the SEM without further sputtering. When comparing cross sections of embedded pillars (Figure 2A, B main text) with the fracture faces (**Figure S2**) it is clear that all three preparation approaches can show the different degrees of porosity. However, since the fracture faces are very uneven, it is not possible to extract meaningful pore sizes.

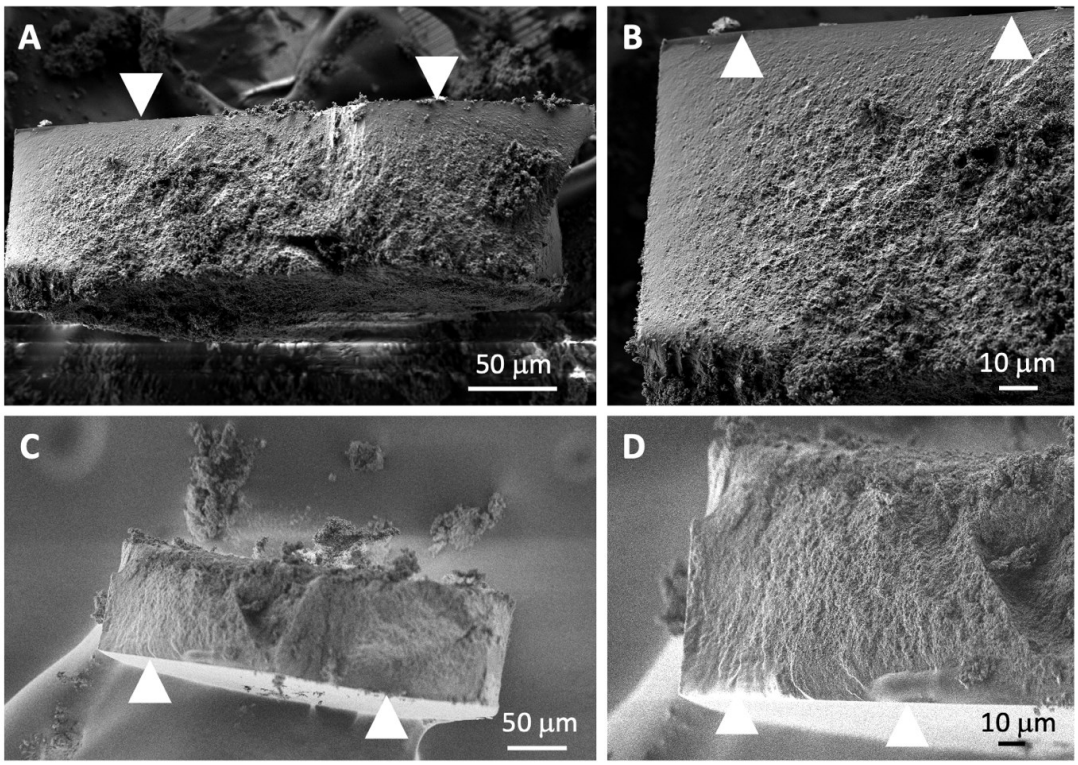

Figure S2. Fracture faces of porous polymer cylinders broken open after staining with OsO_4 (A, B) or unstained (C, D). Arrowheads indicate the base of pillar where it was attached to the glass slide during printing. Since the samples were imaged without sputter coating charging artifacts are observed in some places. Note the lower porosity at the base and side of the cylinder for both samples.

To visualize the pores formed by phase separation during printing, cross sections of the polymer cylinder were characterized by hierarchical imaging. **Figure S3** illustrates the different steps in that process: First, an overview image (555 nm pixel size) showing two adjacent sections was recorded to identify the section outlines (Figure S3A). To identify the pillar cross section, an overview of an entire section was recorded with 200 nm pixel size (Figure S3B). On this data, a ROI through the center of the pillar was placed and imaged with 30 nm pixel size. It extends from the pillar's flat bottom - that adhered to the glass when printed - to the top which is covered with loose material (figure S3C). Three smaller ROIs, illustrating three different porosities, were placed at the corresponding locations and imaged with 5 nm pixel size (figures S3D-F). **Table 1** summarizes the imagining parameters used for the entire dataset.

Table S1 imaging parameters for hierarchical analysis of cross section shown in figure S3

Data set	ROI size	Pixel size	File size	Imaging time
overview	580 x 608 µm	555 nm	1.1 MB	9 sec
section	400 x 175 µm	200 nm	4.2 MB	1 min
segment	153 x 54 µm	30 nm	25 MB	11 min
Small ROI	14.4 x 15.6 µm	5 nm	12.3 MB	9 min

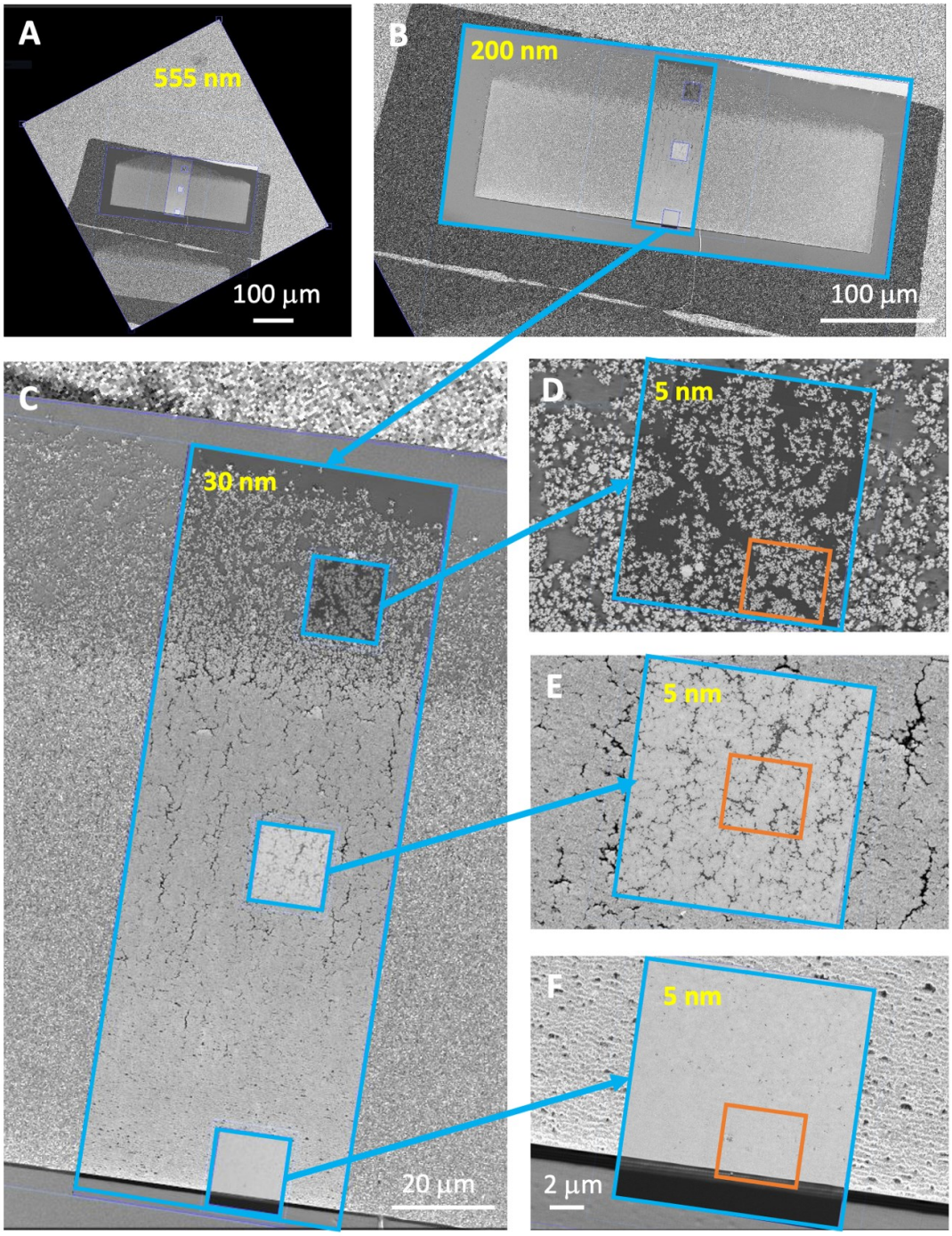

Figure S3. Screenshots from a hierarchical imaging experiment using the Atlas 5 software: Overview A, single section B with position of next imaging ROI, central segment C, small high resolution ROIs D-F. Cyan frames show outlines of the different imaging ROIs, yellow numbers are the pixels sizes used for scanning the corresponding frame. Note that the images shown in the main text (figure 2) are representative clippings (orange frames) from the total data recorded. See also **movie 1** for a zoom-in impression of this dataset.

9. Additional information case study 2

LM imaging of 1045 sections cut from an embedded piece of pyrolized paper origami was done in a hierarchical manner starting with an overview mosaic of one of the three silicon wafer pieces, followed by imaging of its individual ribbons, and finally of corresponding ROIs defined in each section automatically. Time required for one wafer was about 2.5 h, meaning the entire volume could be imaged within one working day. The ribbon images were then imported into the Atlas 5 software for automated SEM imaging and used for navigation there. On two ribbons on wafer 1 (**Figure S4** A) ROIs of 125.7 × 141 µm including the selected feature were placed in each section (figure S4 B) and imaged with SE detectors (pixel size 30 nm). The correlation between the LM appearance of the feature and the higher resolution SEM recording is illustrated by the overlay images C-E.

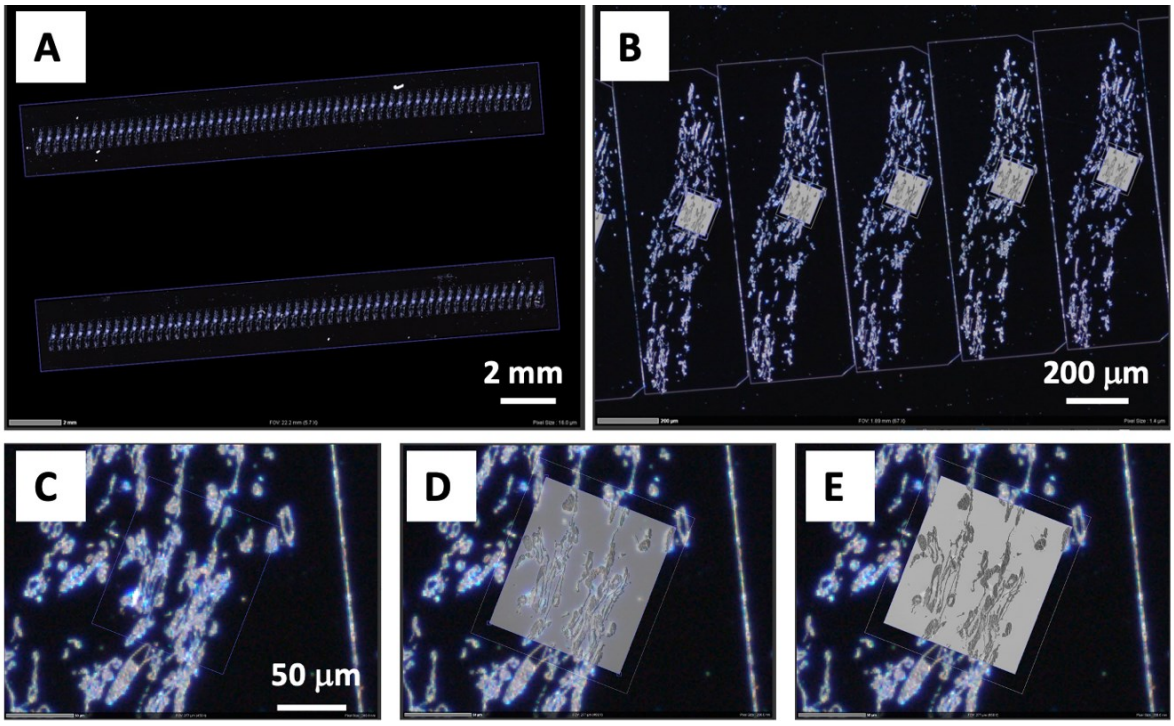

Figure S4. correlation of darkfield LM and SEM on serial sections. Ribbon images from the LM CAT module were imported into the SEM Atlas software (A) and ROIs placed on a selected feature in each section (B). After imaging of all ROIs, a 3D volume of the selected feature was reconstructed (Cf figure 4 F main text). The SEM data are displayed in the structural context of the LM data recorded previously as shown by the overlay images (C-E), presented with different degrees of transparency for the SEM image.

10. Additional information case study 3

To obtain the best possible contrast in the IR-SNOM measurements, far-field spectra of the two pure polymers spin coated on a gold-coated silicon substrate were recorded beforehand. The infrared reflection absorption spectra (IRRAS) are shown in **Figure S5.** For the identification of PMMA the second strongest band at 1152 cm^{-1} was selected, for PS a relatively weak band at 1602 cm^{-1}. The two stronger PS bands between 1400 cm^{-1} and 1500 cm^{-1} cannot be used since PMMA also absorbs at these frequencies. The band at 700 cm^{-1} is not covered by our laser system.

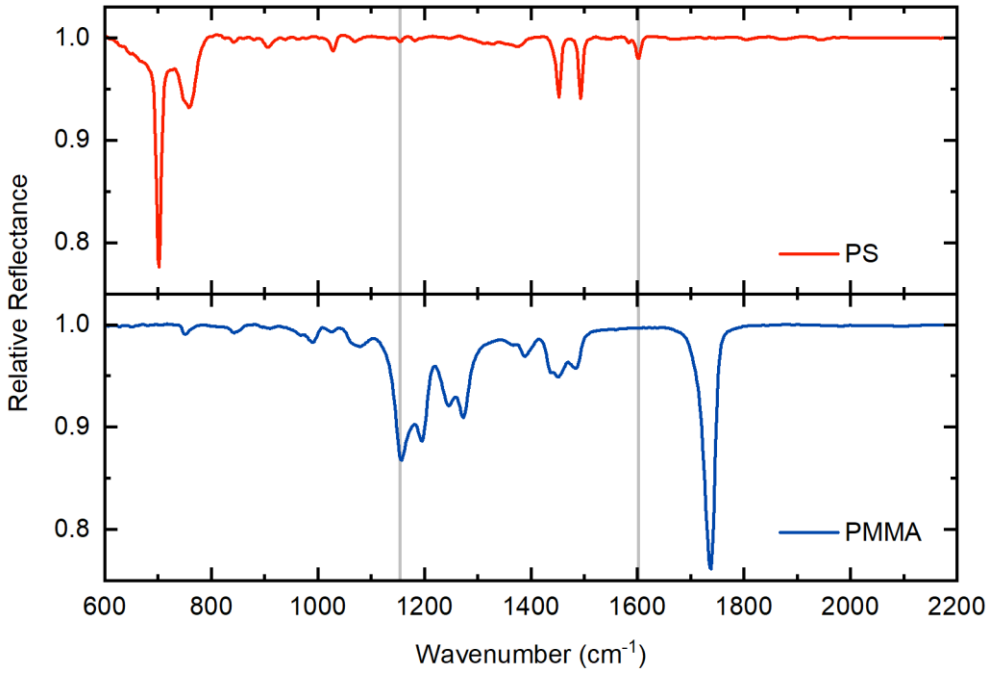

Figure S5. IRRAS spectra of thin films of pure PS and PMMA. The vibrational bands used for the IR-SNOM measurements in the main paper are marked with grey lines.

IR-SNOM is used to measure the topography of the sample in parallel with the optical information. **Figure S6A** shows the topography corresponding to the optical data shown in figure 4 of the main text. The lamellar structure is also observed in the topography. However, an assignment of the materials is only possible through the optical characterization. Figure 6D shows an overlay of the two IR-SNOM phase images (B, C). Registration between the two components was carried out using a descriptor-based registration plugin for ImageJ[5]. First, the two topography images measured simultaneously with the phase images were superimposed. The affine transformation obtained from this step was then applied to the phase images, resulting in their alignment and subsequent superposition.

Another exemplary location of the sample is shown in **Figure S7**. The same kind of structure with lamellae in various orientations and domain boundaries is observed.

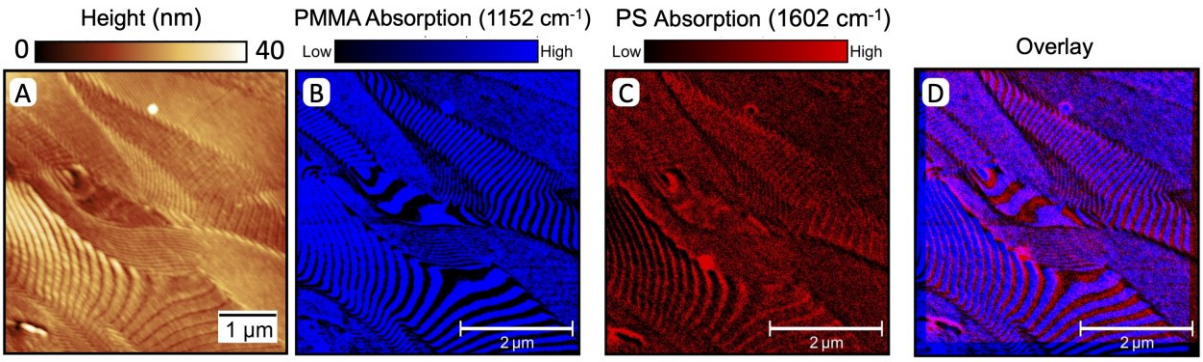

Figure S6. Topography of an ultrathin (70 nm) section of a solvent-annealed PMMA-PS-block-copolymer (A) and construction of the overlay (D) from the corresponding phase images (B, C).

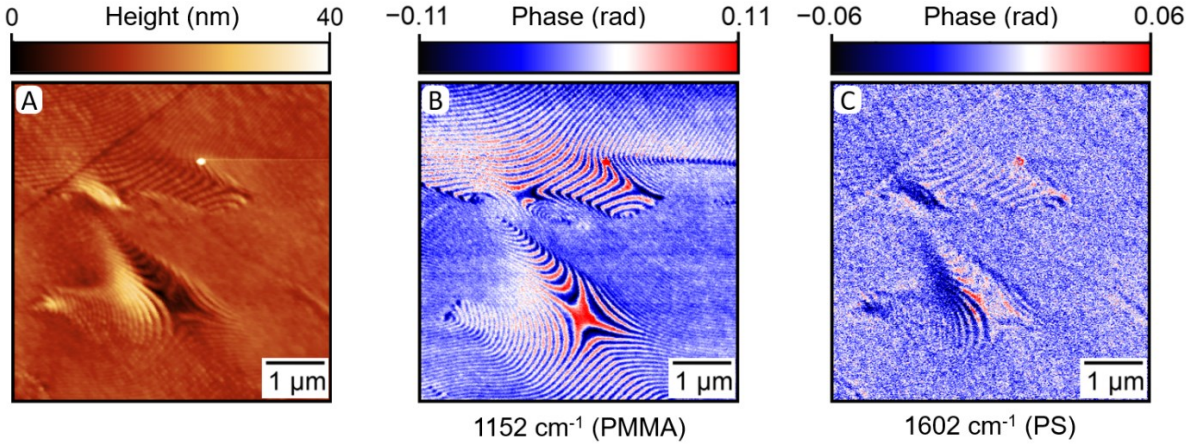

Figure S7. Ultrathin (70 nm) sections of a solvent-annealed PMMA-PS-block-copolymer on a piece of silicon wafer were analyzed with IR-SNOM. Topography (A) and IR-SNOM third-order near-field phase images mapped at 1152 cm^{-1} (B) and 1602 cm^{-1} wavenumber (C) are shown.

Unordered defect zones (cf. Figure 4 main text) appearing dark grey in the SEM image contain both materials, PS and PMMA according to IR-SNOM analysis (Figure S8). However, the material distribution of the two components does not fully overlap.

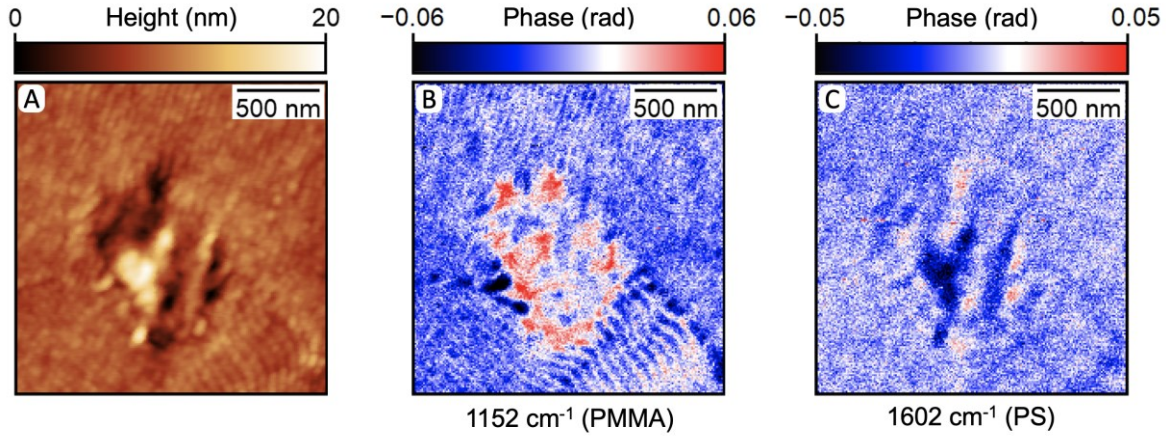

Figure S8. Analysis of an unordered defect zone in a solvent-annealed PMMA-PS-block-copolymer. Topography (A) and IR-SNOM third-order near-field phase images mapped at 1152 cm^{-1} (B) and 1602 cm^{-1} wavenumber (C) are shown.

The relationships between such unordered defect zones and other defects such as faults or transition zones between lamellar zones of different orientation become only clear in 3D. **Figure S9** shows how faults in the lamellar orientation appear in the vicinity of a small unordered defect volume (cf. Figure 4 main text and movie 5).

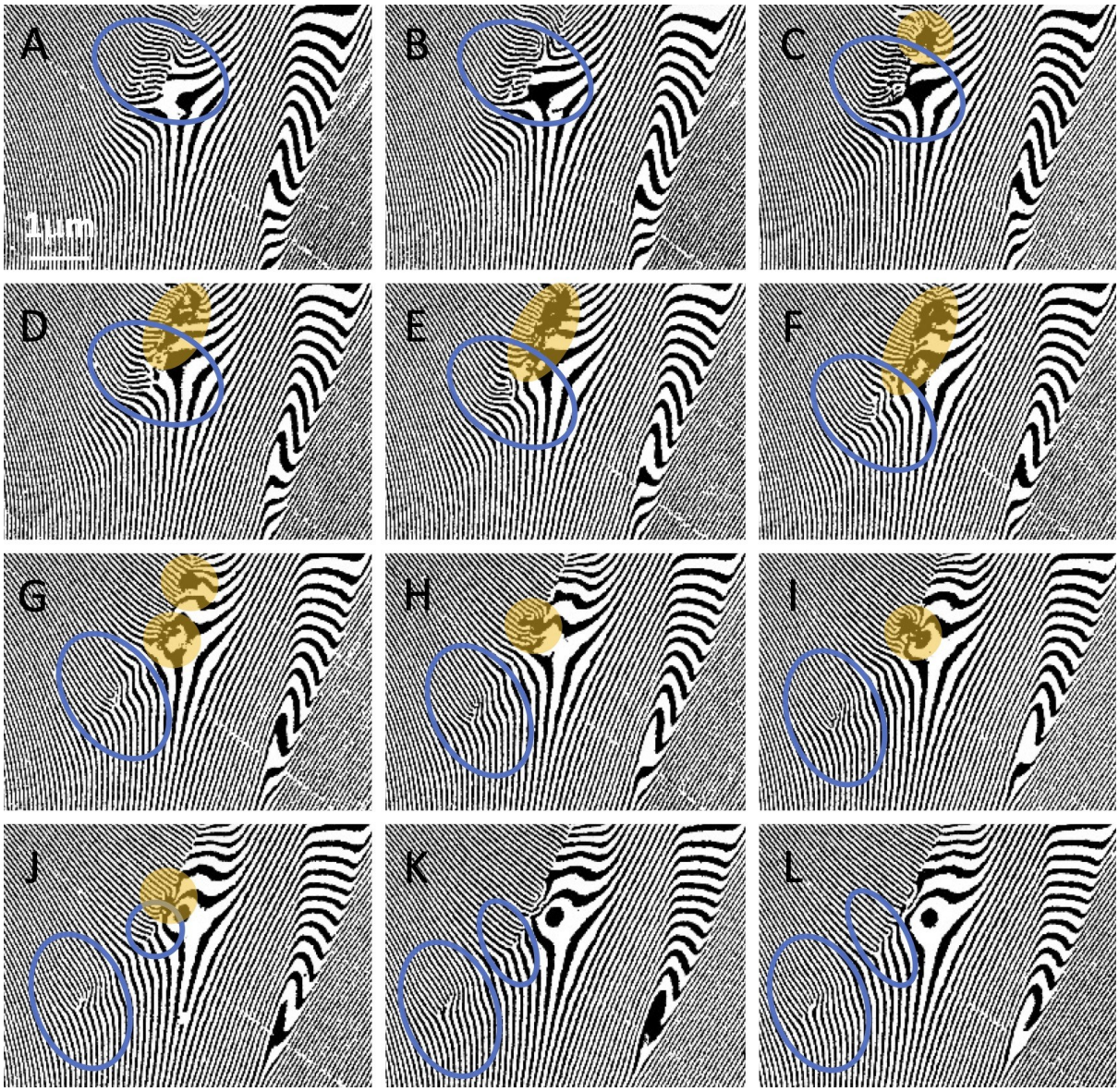

Figure S9. Relationship in 3D of two types of defects. A volume consisting of largely unstructured material (orange overlays, see also movie 5) extending over 8 sections (C-J) is in close contact to faults (blue ovals) within the lamellar zone where lamellae are discontinuous, closed, or appear to branch. These faults are also observed in sections (A, B, K, L) where the first mentioned defect volume is not visible. Furthermore, they are found at an increasing distance from the unstructured material volume (F-L), often with ordered lamellae interspersed between two faults (J-L).

11. Discussion machine learning results case study 4

For the machine learning based segmentation, a shortened ESI dataset from 2 to 11 eV was processed after binning the original 4k images in x and y direction by a factor of 8. The raw and processed data are available from heiDATA (https://doi.org/10.11588/data/LMMXAI). The Principal Component Analysis (PCA) and agglomerative clustering was performed with the python package Scikit-learn 1.2.2[2], Uniform Manifold Approximation and Projection (UMAP) with the python package umap-learn 0.5.3[24 – main text], and MCR-LLM with the python package MCRLLM 0.1.2.[25 – main text]. UMAP was performed with standard parameters, agglomerative clustering with the linkage "ward" and MCR-LLM 100 iterations and the averaged spectra of the epoxide resin and specimen 1 and 2 from the clustering results as initialization.

The dimensionality reduction of the hyperspectral EELS dataset via UMAP (Figure 6A in the main manuscript) reveals four distinct clusters. Dimensionality reduction, e.g., by the popular Principal Component analysis (PCA, **Figure S10**) or by manifold learning algorithms such as UMAP, is a powerful tool to reveal hidden structures in high dimensional datasets (imagine a spectrum with *n* datapoints as a single datapoint in a *n* dimensional space where similar spectra are close to each other) by mapping them to lower dimensions. However, the resulting structures should be assessed with care. In the present case, geometric mixing of the two functional polymers overlapping with the epoxide matrix at the edge of the particles leads to a single cluster between the cluster of the epoxide resin and species 1 instead of the expected two clusters between the epoxide resin and each species. This is caused by the high spectral similarity of the functional polymers in conjunction with the given spectral resolution and noise. The cluster of the spectral mix solely spans between the cluster of the epoxide matrix and the cluster of species 1. This shows that the linear combination of the spectra of the matrix and species 2 is similar to the spectra of species 1. This is illustrated by the occasional misclassification of pixels at the edge of the species 2 particles as species 1, where a certain amount of spectral mixing of the overlapping matrix and species 2 in z direction happens (Figure 6B in the main text). The same effect is observed in the compositional map in Figure 6D in the main manuscript. At the edge of the species 2 particles, a higher content of species 2 is observed by MCR-LLM. A new surface compound, e.g., from the reaction of the epoxy resin with species 2, cannot be completely excluded, but since neither UMAP nor PCA (see Figure S10) indicate the presence of another cluster, the high spectral similarity seems like a more plausible explanation, especially in the context of the slightly noisy MCR-LLM compositional maps with contributions from both functional polymers in all microspheres and the epon matrix in Figure 6D-F. The apparent presence of the three species in all microspheres and the epon matrix indicates an incomplete demixing of the three components. However, since the PCA cannot recover more than 2 significant components (or eigenspectra) the quantitative compositional analysis by MCR-LLM is comparably impressive and gives a good estimate of the chemical composition.

With respect to the MCR-LLM, we would like to mention, that we achieved the best results for the presented dataset by using the averaged spectra from the UMAP clusters as initialization

of the algorithm. However, when applying it to other datasets of the same material, the in MCR-LLM included initializations have in some cases yielded better results.

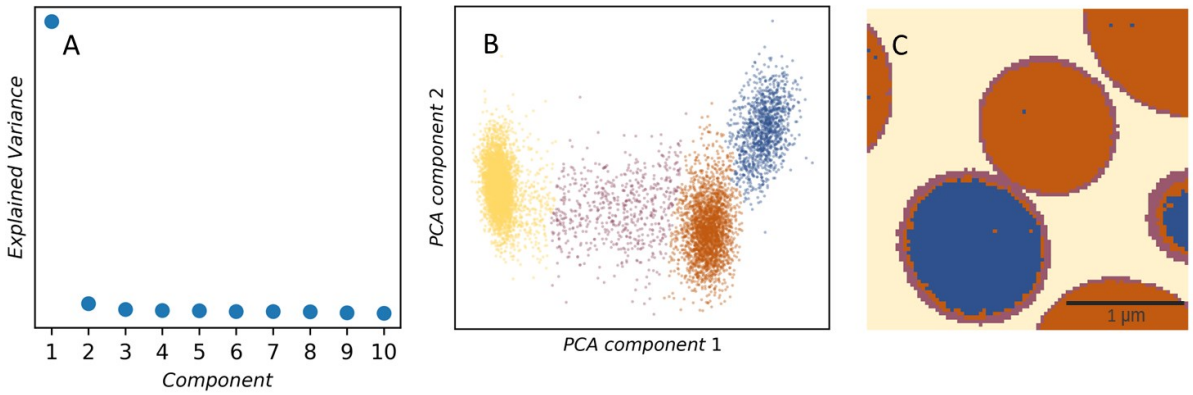

Figure S10 Dimensionality reduction by PCA with scree plot (A) showing maximal two significant components and four clusters (B) for the epoxide matrix (yellow), species 1 (brown), species 2 (blue) and the overlapping areas of the epoxide matrix with species 1 or 2 (purple). The analysis by PCA yields a similar classification (C) as by UMAP (Figure 6 in the main manuscript) but seems to misclassify the mixed spectra containing contributions from the epoxy resin and species 2 at the edge of the particles more often than species 1.

12. References

[1] G. Benner, E. Essers, B. Huber, G. Lang, M. Matijevic, A. Orchowski, W. D. Rau, B. Schindler, P. Schlossmacher, A. Thesen, Microsc Microanal **2004**, 10, 860.

[2] F. Pedregosa, G. Varoquaux, A. Gramfort, V. Michel, B. Thirion, O. Grisel, M. Blondel, P. Prettenhofer, R. Weiss, V. Dubourg, J. Vanderplas, A. Passos, D. Cournapeau, M. Brucher, M. Perrot, E. Duchesnay, JMLR **2011**, 12, 2825.

[3] N. Ocelic, A. Huber, R. Hillenbrand, Appl Phys Lett **2006**, 89, 101124.

[4] I. Wacker, C. Dittmayer, M. Thaler, R. Schröder, in *Volume Microscopy*, Springer Neuromethods Vol. 155, (Eds: I. Wacker, E. Hummel, S. Burgold, R. Schröder), Humana Press, New York, USA, **2020**, Ch. 6.

[5] S. Preibisch, S. Saalfeld, J. Schindelin, P. Tomancak, Nat. Methods **2010**, 7, 418.

[6] Community, B. O. (2018). *Blender - a 3D modelling and rendering package*. Stichting Blender Foundation, Amsterdam. Retrieved from http://www.blender.org

13. List of movies

Movie 1. Hierarchical imaging, case study1. Shown is a zooming in on a cross section of a porous polymer cylinder to regions of interest recorded in an SEM with different pixel sizes.

Movie 2. 3D renderings from an Array tomography dataset, case study 1. Slicing through two sub-volumes from porous objects that had been fabricated by 3D laser microprinting using different laser power.

Movie 3. 3D rendering of data from pyrolized cellulose paper origami, case study 2. Light microscopy data from1045 serial sections recorded in darkfield mode.

Movie 4. 3D rendering of a sub-volume from pyrolized cellulose paper origami, case study 2. SEM data of 110 serial sections selected from a light microscopy dataset of 1045 sections (movie 3).

Movie 5. Segmented defect (yellow) consisting of unordered material in a block co-polymer, case study 3. Faults within lamellar domains (blue ovals) appear in the direct vicinity of the defect.

14. List of additional files

File supportingstructure.blend. Description of fork used in case study 2 in Blender[6] format.

File supportingstructure.stl. Description of fork used in case study 2 in common CAD .stl format.